Study of the $K^+ \to \pi^+ \nu \bar{\nu}$ decay in the momentum region $P_\pi < 199$ MeV/c

A.V. Artamonov,[1] B. Bassalleck,[2] B. Bhuyan,[3, *] E.W. Blackmore,[4] D.A. Bryman,[5] S. Chen,[6, 4] I-H. Chiang,[3]
I.-A. Christidi,[7, †] P.S. Cooper,[8] M.V. Diwan,[3] J.S. Frank,[3] T. Fujiwara,[9] J. Hu,[4] J. Ives,[5] D.E. Jaffe,[3]
S. Kabe,[10] S.H. Kettell,[3] M.M. Khabibullin,[11] A.N. Khotjantsev,[11] P. Kitching,[12] M. Kobayashi,[10]
T.K. Komatsubara,[10] A. Konaka,[4] A.P. Kozhevnikov,[1] Yu.G. Kudenko,[11] A. Kushnirenko,[8, ‡] L.G. Landsberg,[1, §]
B. Lewis,[2] K.K. Li,[3] L.S. Littenberg,[3] J.A. Macdonald,[4, §] J. Mildenberger,[4] O.V. Mineev,[11] M. Miyajima,[13]
K. Mizouchi,[9] V.A. Mukhin,[1] N. Muramatsu,[14] T. Nakano,[14] M. Nomachi,[15] T. Nomura,[9] T. Numao,[4]
V.F. Obraztsov,[1] K. Omata,[10] D.I. Patalakha,[1] S.V. Petrenko,[1] R. Poutissou,[4] E.J. Ramberg,[8] G. Redlinger,[3]
T. Sato,[10] T. Sekiguchi,[10] T. Shinkawa,[16] R.C. Strand,[3] S. Sugimoto,[10] Y. Tamagawa,[13] R. Tschirhart,[8]
T. Tsunemi,[10, ¶] D.V. Vavilov,[1] B. Viren,[3] Zhe Wang,[6, 3] N.V. Yershov,[11] Y. Yoshimura,[10] and T. Yoshioka[10]

(E949 Collaboration)

[1] *Institute for High Energy Physics, Protvino, Moscow Region, 142 280, Russia*
[2] *Department of Physics and Astronomy, University of New Mexico, Albuquerque, NM 87131*
[3] *Brookhaven National Laboratory, Upton, NY 11973*
[4] *TRIUMF, 4004 Wesbrook Mall, Vancouver, British Columbia, Canada V6T 2A3*
[5] *Department of Physics and Astronomy, University of British Columbia, Vancouver, British Columbia, Canada V6T 1Z1*
[6] *Department of Engineering Physics, Tsinghua University, Beijing 100084, China*
[7] *Department of Physics and Astronomy, Stony Brook University, Stony Brook, NY 11794*
[8] *Fermi National Accelerator Laboratory, Batavia, IL 60510*
[9] *Department of Physics, Kyoto University, Sakyo-ku, Kyoto 606-8502, Japan*
[10] *High Energy Accelerator Research Organization (KEK), Oho, Tsukuba, Ibaraki 305-0801, Japan*
[11] *Institute for Nuclear Research RAS, 60 October Revolution Prospect 7a, 117312 Moscow, Russia*
[12] *Centre for Subatomic Research, University of Alberta, Edmonton, Canada T6G 2N5*
[13] *Department of Applied Physics, Fukui University, 3-9-1 Bunkyo, Fukui, Fukui 910-8507, Japan*
[14] *Research Center for Nuclear Physics, Osaka University,*
10-1 Mihogaoka, Ibaraki, Osaka 567-0047, Japan
[15] *Laboratory of Nuclear Studies, Osaka University,*
1-1 Machikaneyama, Toyonaka, Osaka 560-0043, Japan
[16] *Department of Applied Physics, National Defense Academy, Yokosuka, Kanagawa 239-8686, Japan*
(Dated: December 4, 2008)

Experiment E949 at Brookhaven National Laboratory has observed three candidate events for the decay $K^+ \to \pi^+ \nu \bar{\nu}$ in the pion momentum region $140 < P_\pi < 199$ MeV/c in a exposure of 1.71×10^{12} stopped kaons with an estimated total background of 0.93 ± 0.17(stat.)$^{+0.32}_{-0.24}$(syst.) events. Combination of this observation with previous results, assuming a pion spectrum as predicted by the standard model, produces a branching fraction of $\mathcal{B} = (1.73^{+1.15}_{-1.05}) \times 10^{-10}$. We also give the interpretation of the combined results for alternative model of the decay $K^+ \to \pi^+ + nothing$.

PACS numbers:

I. INTRODUCTION

This article is a more detailed report of the recently published final results of experiment E949 at Brookhaven National Laboratory of the study of $K^+ \to \pi^+ \nu \bar{\nu}$ in the pion momentum region $P_\pi < 199$ MeV/c [1]. The observation of $K^+ \to \pi^+ + nothing$ is evaluated within the framework of the standard model and in terms of alternative models.

A. Interpretation of the decay $K^+ \to \pi^+ + nothing$

The only significant standard model (SM) contribution to $K^+ \to \pi^+ + nothing$ is $K^+ \to \pi^+ \nu \bar{\nu}$ where $\nu \bar{\nu}$ is $\nu_e \bar{\nu}_e$, $\nu_\mu \bar{\nu}_\mu$ or $\nu_\tau \bar{\nu}_\tau$. Over the years there have been many alternatives suggested, including (i) new physical mechanisms contributing to $K^+ \to \pi^+ \nu \bar{\nu}$ with the usual neutrino-antineutrino pairs. (ii) cases in which the neutrino flavor is not conserved, (iii) those in which a single unseen particle recoils against the π^+ and (iv) more exotic possibilities.

1. $K^+ \to \pi^+\nu\bar{\nu}$ in the Standard Model

$K^+ \to \pi^+\nu\bar{\nu}$ in the standard model has been thoroughly discussed in Ref. [2]. The story has been one of continual theoretical refinement and experimental narrowing of the relevant parameters since the first modern treatment of this process [3]. A recent assessment of the prediction for the branching ratio of this process is $(0.85 \pm 0.07) \times 10^{-10}$ [4] where the quoted uncertainty is dominated by the CKM matrix elements [5, 6].

This reference included new small corrections to the charm quark contributions to the SM branching ratio.

2. New physics contributions to $K^+ \to \pi^+\nu\bar{\nu}$

Nearly every model of new physics predicts a deviation from the Standard Model prediction for $K^+ \to \pi^+\nu\bar{\nu}$. A summary of these current through mid-2007 can be found in the review of Buras, Uhlig, and Schwab [7]. Since that time there have been new calculations of the branching ratio in the littlest Higgs model with T-parity [8, 9] the possible effects on the branching ratio of a heavy singlet up-quark [10] and a reassessment of the constraints of the Minimal Flavor Violation Model [11].

3. Cases in which the neutrino flavor is not conserved

There are examples stemming from extended Technicolor [12], SUSY [13], and new effective four-fermion interactions involving neutrinos [14]. Like most examples of lepton flavor violation in kaon decay, these tend to be small, but there are cases such as some types of R-violating SUSY [15], in which $K^+ \to \pi^+\nu\bar{\nu}$ gives the limiting constraint on some of the couplings.

4. Cases in which a single particle recoils against the π^+

These include species of axions [16], the familon [17], sgoldstinos[18], a gauge boson corresponding to a new U'(1) group [19, 20], and various light dark matter candidates [21–23]. In general these models do not predict branching ratios as much as use $K^+ \to \pi^+ + nothing$ results to constrain their parameters.

5. More exotic possibilities

These include the effects of "unparticles", which can change the SM π^+ energy spectrum as well as the branching ratio [24].
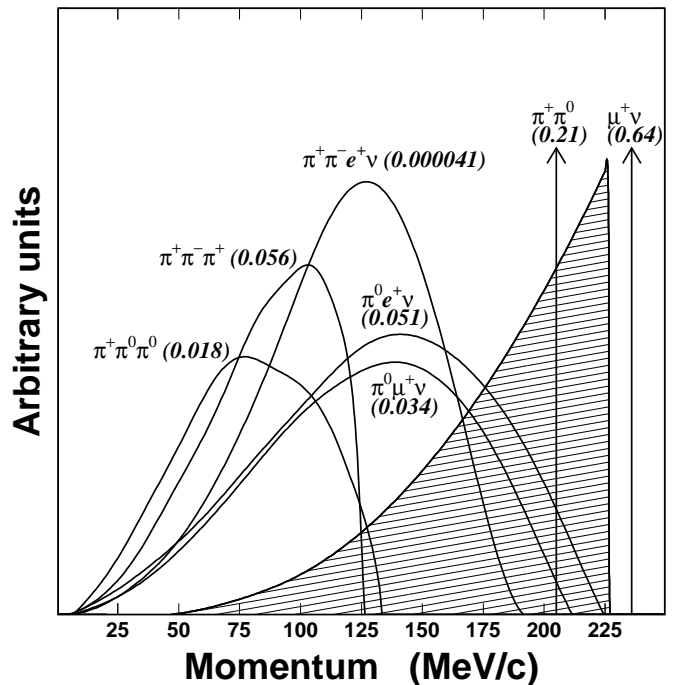

FIG. 1: Momentum spectra of charged particles from K^+ decay in the rest frame. The values in parentheses represent the branching fractions of the decay modes [25]. The hatched spectrum represents the π^+ spectrum from $K^+ \to \pi^+\nu\bar{\nu}$ decay assuming the $V - A$ interaction.

B. Previous results on $K^+ \to \pi^+\nu\bar{\nu}$ below the $K_{\pi2}$ peak

A detailed discussion of the history of measurements of $K^+ \to \pi^+\nu\bar{\nu}$ was given in [2]. However most of these measurements were made in the kinematic region in which the π^+ is more energetic than the π^+ from the background reaction $K^+ \to \pi^+\pi^0$ $(K_{\pi2})$, the so-called "$\pi\nu\bar{\nu}(1)$" region. By contrast very few measurements have been made in the "$\pi\nu\bar{\nu}(2)$" region in which the π^+ is less energetic than that from $K_{\pi2}$ (Figure 1). As will be discussed below, this region is experimentally more challenging than the $\pi\nu\bar{\nu}(1)$ region for a stopped-kaon geometry principally because the π^+ from $K_{\pi2}$ decay can enter the $\pi\nu\bar{\nu}(2)$ region if it undergoes a nuclear interaction in the stopping target.

Among the examples of $\pi\nu\bar{\nu}(2)$ measurements was the first attempt to measure $K^+ \to \pi^+\nu\bar{\nu}$, a heavy liquid bubble chamber experiment [26, 27] at the Argonne Zero Gradient Synchrotron, that was sensitive almost entirely to pion momenta below 200 MeV/c. This experiment achieved a 90% confidence level (CL) limit on the branching ratio of 5.7×10^{-5}, assuming a pure vector spectrum for the π^+. They also extracted limits under the assumptions of tensor and scalar spectra. These were 3.1×10^{-5} and 2.3×10^{-5}, respectively.

Some features of the bubble chamber experiment are notable. The experiment relied on positive π^+ identi-

fication by observation of the $\pi \to \mu \to e$ decay chain. No timing information was available and they relied upon kinematic information, specifically the measured range of the π^+ and the angle between the incoming K^+ and outgoing π^+, to reject background due to K^+ decay-in-flight. They also discarded any events that showed evidence of a π^+-nucleus interactions in the form of a drastic change in ionization along the π^+ track or a kink in the π^+ trajectory. The photon veto with a stated inefficiency of 0.02 for π^0 decay products provided additional background suppression.

There followed a series of counter experiments by a Chicago-Berkeley group that included a measurement in the range $142.7 \mathrm{MeV}/c < p_{\pi^+} < 200.9$ MeV/c [28]. This yielded a 90% CL upper limit on the branching ratio of 9.4×10^{-7} assuming a vector spectrum. They also extracted the corresponding limits for a tensor spectrum, 7.7×10^{-7}, a scalar spectrum, 1.1×10^{-6} and for several other possible shapes.

In contrast to the bubble chamber experiment, the counter experiment made use of a delayed coincidence of 3.3 ns between the outgoing track and the stopped K^+ to suppress beam-related background including K^+ decay-in-flight. They also employed a hermetic 4-π sr photon detector ~ 10 radiation lengths thick (4.3 radiation lengths along the incoming beam channel) that achieved a measured inefficiency for π^0 detection of $< 2.2 \times 10^{-5}$ at 90% CL for identified $K_{\pi2}$ decays [29]. As with the bubble chamber experiment, the $\pi \to \mu \to e$ chain was used for positive π^+ identification and the measured range of the π^+ provided the kinematic information used in the analysis.

The next attempt at a measurement in the $\pi\nu\bar{\nu}(2)$ emerged out of the first phase of the E787 experiment at Brookhaven National Laboratory [30]. This experiment obtained a 90% CL upper limit of 1.7×10^{-8}, assuming a vector spectrum modified by a form factor obtained from $K^+ \to \pi^0 e^+ \nu$ data [31]. We henceforth refer to this form as the "standard model" interaction. E787 also obtained limits of 1.4×10^{-8} and 2.2×10^{-8}, respectively, assuming pure tensor and scalar interactions using their $\pi\nu\bar{\nu}(2)$ data exclusively [32]. Adding their $\pi\nu\bar{\nu}(1)$ data, they were able to improve these limits to 1.0×10^{-8} and 1.8×10^{-8}, respectively [33].

The second generation of this experiment improved the SM limit in the $\pi\nu\bar{\nu}(2)$ region to 4.2×10^{-9}[34] and subsequently to 2.2×10^{-9}[35]. Assuming tensor and scalar interactions E787 ultimately obtained limits of 1.8×10^{-9} and 2.7×10^{-9}, respectively [36].

The E787 detector utilized and built upon concepts from the earlier experiments. Precision measurements of the π^+ kinetic energy and momentum augmented pion identification by range and the $\pi \to \mu \to e$ decay chain. Timing information was used to suppress beam-related backgrounds and kaons were stopped in an active scintillating fiber target. A hermetic 4-π sr detector ~ 14 radiation lengths thick was employed for photon detection. The E787 detector was upgraded in 1999-2000 to

create the successor experiment E949 [37].

II. THE E949 DETECTOR

A. Detector description

An extensive and detailed description of experiment E949 at Brookhaven National Laboratory has been provided elsewhere [2]. In this Section we provide a summary description of the detector and emphasize the features essential to the analysis of data in the $\pi\nu\bar{\nu}(2)$ region.

E949 used an incident 710 MeV/c K^+ beam that was slowed and stopped in the scintillating fiber target as shown schematically in Figure 2. Observation of the decay $K^+ \to \pi^+\nu\bar{\nu}$ requires detection of the incoming K^+ and outgoing π^+ in the absence of any other coincident activity. The charged pion was identified kinematically
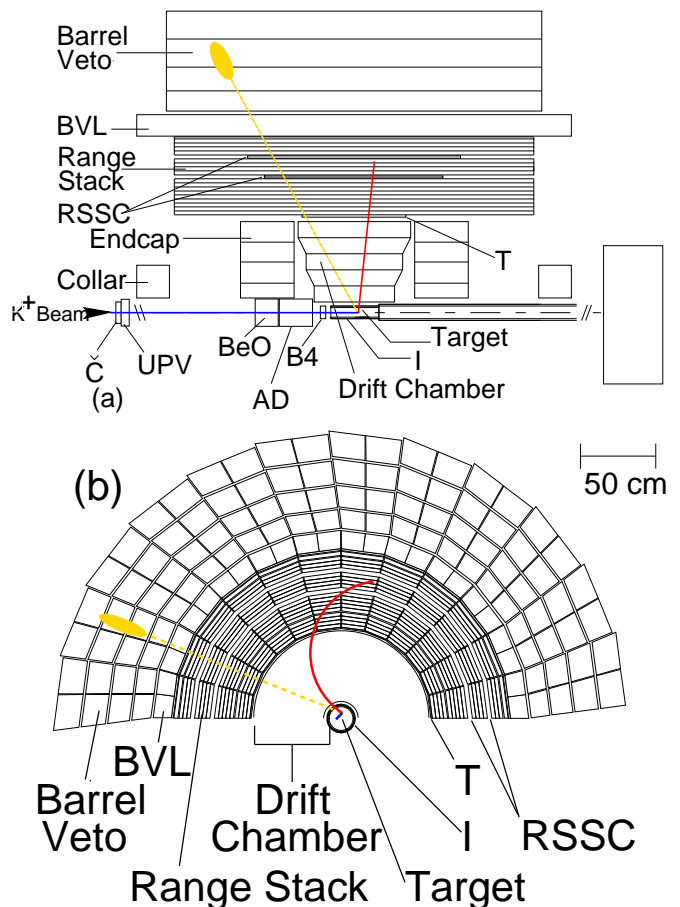
FIG. 2: Schematic side (a) and end (b) views of the upper half of the E949 detector. An incoming K^+ is shown traversing the beam instrumentation, stopping in the target and decaying to $\pi^+\pi^0$. The outgoing charged pion and one photon from the $\pi^0 \to \gamma\gamma$ decay are illustrated. Elements of the detector are described in the text.

by energy (E_π), momentum (P_π) and range (R_π) measurements and by observation of the $\pi \to \mu \to e$ decay

sequence. Since the $K^+ \to \pi^+\nu\bar{\nu}$ branching fraction was expected to be at the 10^{-10} level, the detector was designed to have powerful π^+ identification to reject backgrounds from $K^+ \to \mu^+\nu_\mu$ ($K_{\mu 2}$), $K^+ \to \mu^+\nu_\mu\gamma$ and $K^+ \to \mu^+\pi^0\nu_\mu$, photon detection coverage over 4-π solid angle to reject $K^+ \to \pi^+\pi^0$ and $K^+ \to \pi^+\pi^0\gamma$, and efficient identification of a single incoming K^+ to suppress beam-related background.

E949 employed a right-handed Cartesian coordinate system with $+z$ in the incident beam direction, $+y$ vertically upward and the polar angle θ defined with respect to the $+z$ axis. The entire spectrometer was immersed in a 1 T solenoidal magnetic field in the $+z$ direction.

The incoming charged-particle beam contained approximately three K^+ for every π^+ and traversed a Čerenkov counter (Č), two beam wire proportional chambers (BWPCs), a passive BeO degrader, an active degrader (AD) and a beam hodoscope (B4) as shown in Figure 2. Typically 1.6×10^6 kaons per second entered the target during a 2.2 s spill. The BWPCs are not explicitly shown in the figure. Čerenkov photons emitted by an incoming K^+ (π^+) passing through a lucite radiator were transmitted (internally reflected) into 14 "kaon" ("pion") photomultiplier tubes (PMTs) to form C_K (C_π) coincidences. The PMT signals are split and fed to analog-to-digital converters (ADCs), time-to-digital converters (TDCs) and amplified by ten and sent to 500 MHz charge-coupled devices (CCDs) [38]. The first (second) BWPC station was located downstream of the Čerenkov counter at 168.5 (68.5) cm from the target entrance. Each BWPC station contained three planes with sense wires in the vertical and $\pm 45°$ to the vertical direction. The wire spacing in the first (second) station was 1.27 (0.80) cm. The BWPCs enabled detection of multiple beam particles. The degraders were designed such that incident kaons stopped within the fiducial volume of the scintillating fiber target. The AD consisted of 40 layers of 2-mm plastic scintillator (13.9 cm diameter) interleaved with 39 2.2-mm thick copper disks (13.6 cm diameter) azimuthally divided into 12 sectors that were coupled by wavelength-shifting (WLS) fibers to PMTs that were read out by ADCs, TDCs and CCDs. These devices enabled measurement of activity in the AD coincident with the incoming beam and outgoing products of K^+ decays. The B4 hodoscope downstream of the AD had two planes of 16 segmented plastic scintillator counters with 7.2-mm pitch oriented at $\pm 33.5°$ with respect to the horizontal direction. The cross-section of each counter was in a "Z" shape to minimize inactive area seen by the beam and to improve the spatial resolution. Each counter was connected to a PMT by three WLS fibers and each PMT was read out by ADCs, TDCs and CCDs. The B4 enabled a measurement of the target entry position of the beam particle as well as identification of the incident particle by energy loss.

The target was composed of 413 scintillating fibers 3.1-m long with a 5-mm square cross-section packed to form a 12-cm-diameter cylinder. A number of smaller (1-, 2-, and 3.5-mm square) "edge" fibers filled the gaps at the outer edge of the target. Each 5-mm fiber was connected to a PMT and the output PMT signals were split and input into an ADC, TDC, low-gain($\times 1$) and high-gain($\times 3$) CCD. Multiple edge fibers were ganged onto 16 PMTs with similar readout. Analysis of the 500 MHz sampling information provided by the target CCDs was essential for isolating and suppressing backgrounds in the $\pi\nu\bar{\nu}(2)$ region. Two cylindrical layers of six plastic-scintillation counters defined the fiducial volume of the target. The inner layer of counters (dubbed "I counters" or "ICs") were 6.4-mm thick with an inner radius of 6.0 cm and extended 24 cm from the upstream end of the target. The 5-mm thick outer scintillation counters (VC) overlapped the downstream end of the ICs by 6 mm and extended 196 cm further downstream. The VC served to veto particles that exited the target downstream of the IC. Each IC and VC element was instrumented with a PMT and readout by an ADC, a TDC and a 500 MHz transient digitizer(TD) [39].

The origin of the E949 coordinate system was the center of the cylindrical volume defined by the ICs. This point also coincided with the center of the drift chamber.

The drift chamber, also called the "ultra thin chamber" (UTC) [40], was located just outside the IC and inside the range stack as shown in Figure 2. The UTC extended radially from 7.85 cm to 43.31 cm and served to measure the trajectory and momentum of the charged track from the target to the range stack. Each of the three superlayers of the UTC contained four layers of axial anode wires that provided xy position information between two cathode foil strips that provided z position information. Beginning at an inner radius of 45 cm, the range stack consisted of 19 layers of plastic scintillator counters and staggered double-layer straw chambers (RSSC) embedded after the 10th and 14th layers of scintillator. The range stack enabled the measurement of the range and energy of the charged particle, the observation of the $\pi \to \mu \to e$ decay sequence and the measurement of photon activity. The 19 layers of plastic scintillator counters were azimuthally segmented into 24 sectors as shown in Figure 2. Layers 2-18(19) were 1.9(1.0)-cm thick and 182 cm long and were coupled on both ends to PMTs with lucite light guides. The trigger counters (T counters) in the innermost layer served to define the fiducial volume for K^+ decay products and were 6.4-mm thick and 52-cm long counters coupled to PMTs on both ends by WLS fibers. The T counters were thinner than layers 2-19 to suppress rate due to photon conversions. Signals from each range stack PMT were passively split 1:2:2 for ADCs, discriminators and fan-in modules. The discriminator output was sent to TDCs and used in the trigger. The fanned-in analog sum of 4 PMTs in four adjacent sectors (dubbed a range stack "hextant") was fed into a single TD and provided to the trigger. The TDs sampled and digitized the charge in 2 ns intervals with an 8-bit resolution. The 500 MHz sampling was sufficient to resolve a $\pi^+ \to \mu^+$ decay with a 5-ns separation between

the stopped pion and the emitted muon.

Identification of $K^+ \to \pi^+\nu\bar{\nu}$ decays required detection of any activity coincident with the charged track. Photons from $K_{\pi 2}$ and radiative kaon decays were detected in a hermetic photon veto system with 4-π sr solid angle coverage as shown in Figure 2. Except for the end caps, all photon veto detectors were lead-scintillator sandwich-style electromagnetic calorimeters. Essentially every scintillation counter in the experiment served as a photon veto detector. The barrel veto (BV) and barrel veto liner (BVL) covered 2/3 of 4-π sr in the barrel outside the range stack with a thickness 14.3 and 2.29 radiation lengths (r.l.) at normal incidence, respectively. The downstream and upstream end caps (EC) consisted of 13.5 r.l. thick undoped cesium iodide crystals and covered approximately 1/3 of 4-π sr [41, 42]. The upstream photon veto (UPV) was 3.1 r.l. thick and was mounted just downstream of the Čerenkov counter with an inner hole for the beam. The upstream and downstream collar (CO) counters shown in Figure 2 provided approximately 4.5 and 9 r.l. at normal incidence, respectively. An additional collar counter (μCO) was installed downstream of the downstream CO between the inner face of the magnet end plate and the target [2]. The downstream photon veto (DPV) provided up to 7.3 r.l. of coverage downstream of the target, EC and collar. The AD was 6.1 r.l. thick and contributed important photon veto coverage in the poorly instrumented region occupied by the incoming beam. The thickness in radiation lengths of the photon veto system as a function of the cosine of the polar angle is shown in Figure 3

B. Trigger

The trigger system for E949 was designed to select $K^+ \to \pi^+\nu\bar{\nu}$ events from the large number of K^+ decays and scattered beam particles by requirements on the π^+ range, evidence of a $\pi^+ \to \mu^+\nu_\mu$ decay in the range stack, lack of other detector activity at the time of the π^+ and the presence of a K^+ at an appropriately earlier time. The elements and architecture of the two-stage trigger system have been described previously [2]; we describe the features essential for the analysis of the $\pi\nu\bar{\nu}(2)$ region.

The logical OR of the following two signal triggers was used for the $\pi\nu\bar{\nu}(2)$ analysis

$$\pi\nu\bar{\nu}(1) \equiv KB \cdot DC \cdot (T \cdot 2 \cdot IC) \cdot (6_{ct} + 7_{ct}) \cdot \overline{19_{ct}}$$
$$\cdot \overline{zfrf} \cdot L0rr1 \cdot HEX \cdot \overline{(BV + BVL + EC)}$$
$$\cdot L1.1 \cdot L1.2 \qquad (1)$$

$$\pi\nu\bar{\nu}(2) \equiv KB \cdot DC \cdot (T \cdot 2 \cdot IC) \cdot 3_{ct} \cdot 4_{ct} \cdot 5_{ct} \cdot 6_{ct}$$
$$\cdot \overline{(13_{ct} + \cdots 18_{ct})} \cdot \overline{19_{ct}} \cdot L0rr2 \cdot HEX$$
$$\cdot \overline{(BV + BVL + EC)} \cdot L1.1 \cdot L1.2 \ . \qquad (2)$$
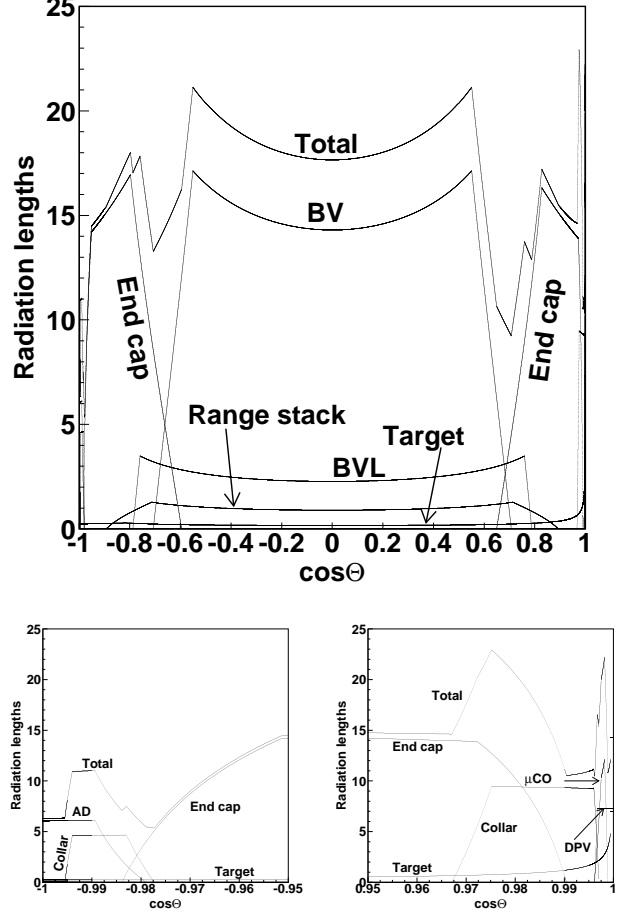

FIG. 3: (Upper) Contribution of each photon veto detector in radiation lengths as a function of $\cos\theta$ for a photon emitted from the origin of the detector coordinate system. (Lower) Contribution of each photon veto element in the upstream and downstream regions with 18° of the beam.

We collectively refer to the OR of the $\pi\nu\bar{\nu}(1)$ and $\pi\nu\bar{\nu}(2)$ triggers as $\pi\nu\bar{\nu}(1+2)$.

The K^+ beam condition KB required a coincidence of at least 5 C_K counters, the B4 hodoscope and at least 20 MeV of deposited energy in the target. The KB signal served as the beam strobe for the trigger. $T \cdot 2 \cdot IC$ required a coincidence of the first two range stack layers in the same sector with at least one IC to ensure that a charged track exited the target and entered the range stack. The delayed coincidence (DC) required the IC time to be at least 1.5 ns later than the C_K coincidence to select kaon decays at rest. The $\pi\nu\bar{\nu}(1)$ trigger condition $\overline{zfrf}$ required the z position of the charged track to be within the fiducial region of all traversed range stack layers. The "ct" designation refers to the range stack $T \cdot 2$ sector and the next two adjacent sectors that would be traversed by a positively charged particle in the magnetic field. For the $\pi\nu\bar{\nu}(2)$ trigger, the charged track requirements $3_{ct} \cdot 4_{ct} \cdot 5_{ct} \cdot 6_{ct} \cdot \overline{(13_{ct} + \cdots 18_{ct})} \cdot \overline{19_{ct}}$ ensured hits

in layers T through 6 to suppress contributions from 3-body K^+ decays and vetoed on hits in the outer layers to suppress long-range charged tracks beyond the $\pi\nu\bar{\nu}(2)$ kinematic region. The BV, BVL, EC and HEX requirements vetoed events with photons in the BV, BVL, EC and range stack, respectively. The $L0rr1$ and $L0rr2$ were refined requirements of the charged track range taking into account the number of target fibers hit and the track's z position in layers 3, 11, 12, 13 as well as the deepest layer of penetration in order to reject long range tracks such as the μ^+ from $K^+ \rightarrow \mu^+\nu_\mu$ decay. The $L1.1$ used the ratio of the height and area of the pulse(s) recorded by the TD to select the two-pulse signature of the $\pi^+ \rightarrow \mu^+$ decay in the range stack counter in which the charged track was determined to have stopped. The $L1.2$ used data digitized by the range stack ADCs to reject events with hits near the stopping counter that could falsely satisfy the $L1.1$ and to reject events with hits in both of the two adjacent hextants when the $T \cdot 2$ and stopping counter were in the same sector. For the final 60.6% of the data taking, an online pion Čerenkov veto was included in the $\pi\nu\bar{\nu}(2)$ trigger due to an increase in the rate of beam pions caused by a beam line malfunction.

A subset of the data selected by the $\pi\nu\bar{\nu}(1+2)$ trigger is shown in Figure 4.

In addition to the $\pi\nu\bar{\nu}(2)$ and $\pi\nu\bar{\nu}(1)$ triggers, additional "monitor" triggers were formed for calibration, monitoring, acceptance and background measurements [2]. The monitor triggers used subsets of the components of the signal trigger to predominantly select events due to $K_{\mu2}$ and $K_{\pi2}$ decays as well as scattered beam pions (π_{scat}). An additional "CEX" monitor trigger requiring two $T \cdot 2$ hits was used to collect events resulting from the charge-exchange process $K^+n \rightarrow pK_S^0$ followed by $K_S^0 \rightarrow \pi^+\pi^-$. Information derived from this CEX monitor data was used as input to simulation to determine the background from charge-exchange as described in Section III C 3. In order to measure the efficiency of the $T \cdot 2 \cdot IC$ condition (Section III D), we also defined a KB monitor trigger that required the KB condition described previously.

III. DATA ANALYSIS

The total kaon exposure for this analysis was 1.71×10^{12} corresponding to 143×10^6 $\pi\nu\bar{\nu}(1+2)$ triggers. The total kaon exposure was slightly less than the 1.77×10^{12} used for the E949 $\pi\nu\bar{\nu}(1)$ analysis because we discarded some data due to more stringent requirements on the reliability of the BWPCs, the Čerenkov counter and the target CCDs.
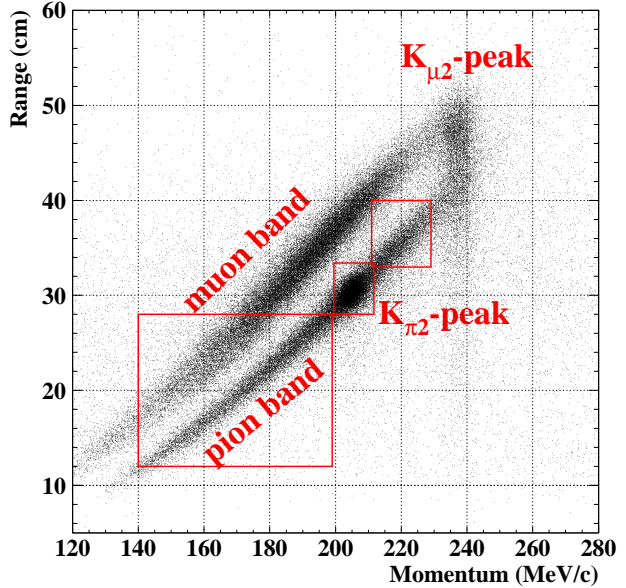

FIG. 4: Range in plastic scintillator *vs.* momentum for charged particles accepted by the $\pi\nu\bar{\nu}(1+2)$ triggers. The concentrations of events due to the two-body decays are labeled $K_{\pi2}$-peak and $K_{\mu2}$-peak. The decays $K^+ \rightarrow \pi^0\mu^+\nu_\mu$ and $K^+ \rightarrow \mu^+\nu_\mu\gamma$ contributed to the muon band. The pion band resulted from $K^+ \rightarrow \pi^+\pi^0\gamma$ decays, $K_{\pi2}$ decays in which the π^+ scattered in the target or range stack and beam π^+ that scatter in the target. The boxes at low and high momentum represent the signal region for this analysis and the previous $\pi\nu\bar{\nu}(1)$ analysis [2], respectively. The selection criteria for the signal region and the $K_{\pi2}$-peak as well as the techniques of identification and suppression of these backgrounds are described in the text. This distribution represents 0.13% of the total kaon exposure.

A. Overview

Identification of the $K^+ \rightarrow \pi^+\nu\bar{\nu}$ decay involved positive observation of the K^+ and daughter π^+ in the absence of coincident detector activity. $K^+ \rightarrow \pi^+\nu\bar{\nu}$ has been studied in two kinematic regions dubbed "$\pi\nu\bar{\nu}(1)$" and "$\pi\nu\bar{\nu}(2)$" that lie above and below the $K_{\pi2}$ peak, respectively (Figures 1 and 4). The $\pi\nu\bar{\nu}(1)$ and $\pi\nu\bar{\nu}(2)$ regions in E949 extended from 211 to 229 MeV/c [2] and 140 to 199 MeV/c in π^+ momentum, respectively. In the $\pi\nu\bar{\nu}(1)$ region, the background was dominated by $K_{\pi2}$, $K_{\mu2}$, $K^+ \rightarrow \mu^+\nu_\mu\gamma$ and $K^+ \rightarrow \pi^0\mu^+\nu_\mu$ decays and was sufficiently suppressed by positive identification of the π^+ based on kinematic properties, observation of the $\pi \rightarrow \mu \rightarrow e$ sequence and by the hermetic photon veto capability [2]. Previous studies [35, 43] in $\pi\nu\bar{\nu}(2)$ region identified the main background as due to $K_{\pi2}$ decays in which the charged pion scatters in the target, loses energy and falls into the signal region above the $K \rightarrow \pi^+\pi^0\pi^0$ endpoint and below the $K_{\pi2}$ peak. Additional lesser sources of kaon decay background with the

π^+ in the $\pi\nu\bar{\nu}(2)$ region included $K^+ \to \pi^+\pi^0\gamma$ ($K_{\pi2\gamma}$) and $K^+ \to \pi^+\pi^- e + \nu_e$ (K_{e4}). Successful analysis of the $\pi\nu\bar{\nu}(2)$ region relied on the photon veto capability and, in contrast to the $\pi\nu\bar{\nu}(1)$ analysis, identification of the scattering process or the presence of additional particles in the target. The $\pi\nu\bar{\nu}(2)$ region has a larger potential acceptance than $\pi\nu\bar{\nu}(1)$ because the phase space is larger and the loss of π^+ due to nuclear interactions in the detector is smaller at lower pion energies. We also gained acceptance by increasing the size of the signal region with respect to the previous analyses [35, 43] These factors partially mitigated the loss of the acceptance due to these additional requirements needed to suppress background.

1. Kaon-decay background

The largest background contribution in the $\pi\nu\bar{\nu}(2)$ region was due to $K_{\pi2}$ decay in which the charged pion experienced a nuclear interaction near the kaon decay point, probably on a carbon nucleus in the plastic scintillator of the target. The reduced kinetic energy due to the scatter put the pion in the $\pi\nu\bar{\nu}(2)$ region. In addition, the scatter obscured the directional correlation between the charged and neutral pions, thus directing the photons from π^0 decay away from the barrel region of the photon veto. This background was suppressed by recognition of the scattering process in the target. A smaller background contribution due to scattering of the charged pion in the range stack was suppressed by the track pattern and energy deposit in the range stack. The photon veto served to suppress these "$K_{\pi2}$-scatter" backgrounds as well as background due to the radiative decay $K_{\pi2\gamma}$. Background due to K_{e4} was suppressed by identification of additional particles in the target. Kaon decays with a muon in the final state, $K_{\mu2}$, $K^+ \to \mu^+\nu_\mu\gamma$ and $K^+ \to \pi^0\mu^+\nu_\mu$, were suppressed by kinematics and the recognition of the $\pi \to \mu \to e$ signature as well as the photon veto for the latter two decays.

2. Beam-related background

The beam-related backgrounds were categorized into single- and double-beam background and CEX background. The CEX background occurred due the production of a K^0 in the target from the charge-exchange process $K^+n \to pK^0$. If the K^0 turned into a K_L^0 that subsequently underwent semileptonic decay, the π^+ could fall in the $\pi\nu\bar{\nu}(2)$ kinematic region. CEX background was rejected by observing the gap between the K^+ and π^+ fibers due to propagation of the non-ionizing K_L^0, by the inconsistency between the energy deposited by the K^+ and the reconstructed z of the outgoing pion and by identification of the accompanying negative lepton. In addition, requirements on the delayed coincidence between the K^+ and π^+ suppressed CEX background due to the short K_L^0 flight time.

Single-beam background could have been due to a K^+ entering the target and decaying in flight to produce a π^+ in the $\pi\nu\bar{\nu}(2)$ region. Incoming beam π^+ misidentified as K^+ and scattering in the target also contributed to the single-beam background. Positive identification of the incoming particle as a kaon as well as requirements on the delayed coincidence between the incoming and outgoing tracks suppressed the single-beam background.

The two processes that contributed to single-beam background, kaon decay-in-flight and pion scattering, formed the double-beam background when preceded by an additional incoming kaon whose decay products were undetected. Double-beam background was suppressed by requiring a lack of activity in the beam and target in coincidence with the π^+ detected in the range stack.

3. Analysis method and strategy

We used analysis procedures and strategies similar to that of the E949 analysis of the $\pi\nu\bar{\nu}(1)$ region [2] with some extensions that took into account the difficulty of isolating some background samples in the data in the $\pi\nu\bar{\nu}(2)$ region. As with the previous analysis, we adopted a "blind" analysis method in that we did not examine the pre-defined signal region until all background and acceptance analysis was completed. Since we also attempted to perform all background estimates directly from the data, we inverted at least one selection criteria ("cut") when we used the $\pi\nu\bar{\nu}(1+2)$ data to avoid examining the signal region. Every third $\pi\nu\bar{\nu}(1+2)$ trigger formed the "1/3" sample that was used to determine the selection criteria. We then obtained unbiased background estimates by applying the finalized selection criteria to the remaining "2/3" sample of $\pi\nu\bar{\nu}(1+2)$ triggers.

The preferred method of background estimation employed the bifurcation method illustrated in Figure 5. The parameter space of two cuts "CUT1" and "CUT2"
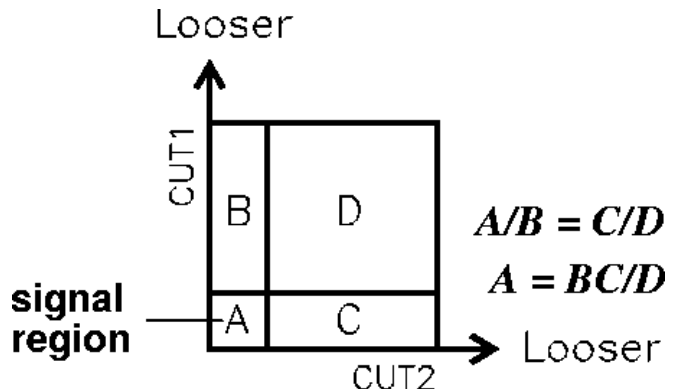

FIG. 5: Schematic of the bifurcation method. The background level in region A can be estimated from the number of events observed in the other regions assuming CUT1 and CUT2 are uncorrelated. See text for details.

can be divided into the four regions shown in the figure

by the application of each cut or the inverted cut. For example, the number of events in the signal region "A" can be determined by application of both CUT1 and CUT2. If the background rejection of CUT1 does not depend on CUT2 and vice versa, then the number of events in A can be estimated as the number of events in region B times the ratio of the number of events in regions C and D or $A = BC/D$. In practice, we employed two branches for the bifurcation analysis. The "normalization branch" analysis was performed to obtain the number of events, N_{norm}, in region B. A "rejection branch" analysis was used to obtain D/C. We defined the rejection as $R \equiv (C + D)/C$ and obtained the background estimate as

$$b = f \times N_{norm}/(R - 1) \qquad (3)$$

where $f = 3(3/2)$ for the $1/3(2/3)$ samples. For all background estimates in this analysis, the normalization branch was taken from the $\pi\nu\bar{\nu}(1+2)$ data. We used the $\pi\nu\bar{\nu}(1+2)$ data to obtain the rejection branch for all backgrounds except for the CEX, K_{e4} and $K_{\pi2\gamma}$ backgrounds that could not be cleanly isolated in data. When no events ($N_{norm} = 0$) were available in the normalization branch, we conservatively assigned $N_{norm} = 1$.

We checked the validity of the background estimates by loosening cuts and comparing the predicted the number of events just outside the signal region with observations (Section III C 8). In addition we examined events passing a single major selection criteria to search for unforeseen background sources and coding mistakes (Section III C 9).

B. Data selection requirements

1. Event reconstruction

Events were reconstructed as described in [2] except as noted below. Event reconstruction was performed in a number of steps consisting of track-fitting in various detector systems such as the beam-line detectors, the range stack, the UTC and the target. Multiple iterations of the track-fitting were performed in many of the detector systems using progressively better information from track-fitting from other detector systems as constraints.

The following discussion focuses on the target track-fitting to clearly define the target-fiber classification scheme for use in the description of the target CCD fitter and descriptions of the cuts using target fiber information. In contrast to the analysis of the $\pi\nu\bar{\nu}(1)$ region [2], the fit to the UTC track did not include information from the target fibers. Performing the target fit separately improved the ability to detect a pion scatter in or near the target.

After the range stack and UTC track fitting were performed, target fibers were clustered into K^+ and π^+ paths based on geometry, energy and timing information as shown in Figure 6. The pion fibers had to lie
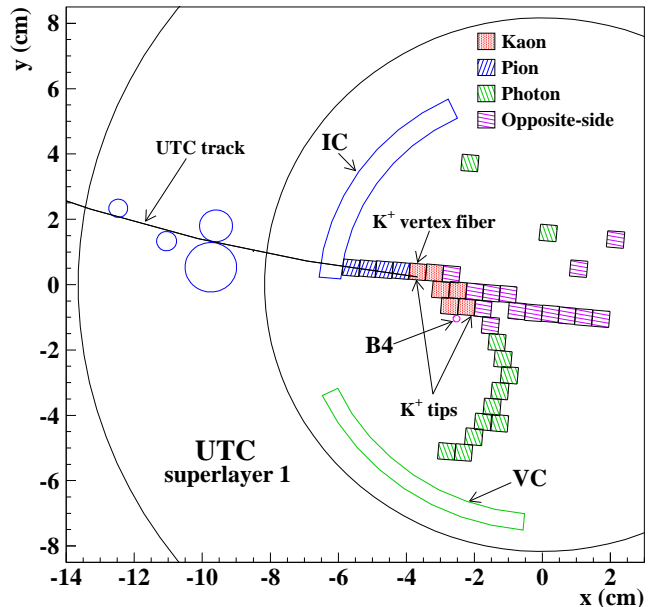

FIG. 6: Example target x-y display showing the assignment of pion, kaon, γ and opposite-side pion fibers as described in the text. The arc that terminates in the reconstructed kaon vertex fiber represents the extrapolated UTC track. The circles on the track represent the UTC hits with the radius giving the drift distance. Only the innermost superlayer of the UTC is shown. The IC and VC elements with hits are indicated. The position of the incoming K^+ as reconstructed by the B4 hodoscope information is also indicated in the figure as are the kaon fiber "tips". This event was selected in the K_{e4} normalization branch (Section III C 2). The measured time, energy and apparent curvature of the contiguous γ fibers are consistent with a positron and the time and energy of the opposite-side pion fibers are consistent with a negative pion. Units are cm.

along a strip (typically 1 cm in width) along the UTC track extrapolated into the target, have an energy between 0.1 and 10.0 MeV and be in coincidence with the reconstructed time of the π^+ in the range stack (t_{RS}). The kaon fibers had to have greater than 4 MeV of energy and be coincident with the beam strobe. Any fiber that did not fall into the K^+ or π^+ fiber categories was classified as a γ fiber if it had more than 0.1 MeV of energy. The K^+ decay vertex fiber was identified as the K^+ fiber closest to the extrapolated UTC track and farthest from the x-y position of the B4 hit. Pion fibers that were located on the opposite side of the decay vertex with respect to the outgoing track were classified as "opposite-side pion" fibers and were possible due to K^+ decays to multiple charged particles or a photon conversion. The energy-weighted average times of the K^+ and π^+ hits were defined as t_K and t_π, respectively. The sums of the K^+ and π^+ energies were defined as E_K and E_π, respectively. The distributions of E_π and E_K are shown in Figure 7.
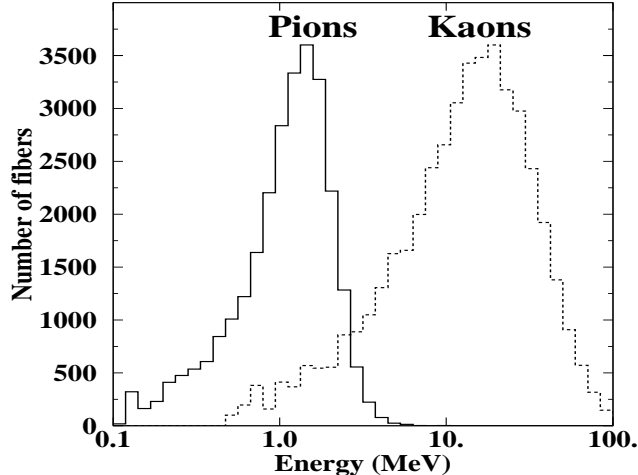
FIG. 7: The energy per pion fiber or kaon fiber in events in the $K_{\pi 2}$-peak in $\pi\nu\bar{\nu}(1+2)$ triggers. The height of the pion energy distribution has been scaled by a factor of 0.31 to be the same as the height of the kaon energy distribution for the purpose of display. The average number of pion (kaon) fibers in the selected events is 10.7 (5.8). Note the logarithmic abscissa.

The identified pion fibers were subjected to a least-squares fit to the hypothesis of positively charged pion track [36]. The "target-track fitter" took into account the x, y positions of each fiber, the consistency with the fitted UTC track, and the observed energy in fibers traversed by the fitted track.

To aid in the identification of pion scattering in the target, the activity in each of the target fibers as recorded by the low-gain and high-gain CCDs (Section II A) was fitted using a single-pulse and a double-pulse hypothesis. For each channel of each fiber a standardized K^+ pulse used for the target CCD fitter was created using kaon fiber data from $K_{\mu 2}$ monitor trigger data. For each fiber having an energy greater than a fiber-dependent threshold, typically 2 (0.5) MeV for low- (high-)gain, the fitting procedure was performed on the low-gain and the high-gain CCD information independently. The first step of the procedure was a least-squares fit to a single-pulse hypothesis for each fiber channel passing the above criteria. The single-pulse fit used two parameters, the pulse amplitude and the time. If the probability of χ^2 ($\mathcal{P}(\chi^2)$) of the single-pulse fit was less than 25%, a double-pulse fit was performed. The double-pulse fit used four parameters, the amplitudes and times for the first and second pulses.

2. Requirements on π^+ in the target

Numerous requirements were placed on the activity in the target to suppress background and ensure reliable determination of the kinematic properties of the charged pion. These requirements were based on the results of the target CCD fitter, the reconstructed energy and time of the pion and kaon fibers, the pattern of kaon and pion fibers relative to information from the rest of the detector and the results of the target-track fitter.

Target pulse data analysis

Detection of pion scattering in the target in the identified kaon fibers required reliable results from the target CCD fitter. For each kaon fiber, the fit results for the high-gain and low-gain channels were examined to determine if $\mathcal{P}(\chi^2) > 5 \times 10^{-5}$ for the double-pulse hypothesis. Next an algorithm determined if the information from the high-gain CCD, the low-gain CCD or a combination of the two should be used for each fiber with an acceptable double-pulse fit. The algorithm was based on the energy in the kaon fiber as measured by the ADC and by the time difference $t_\pi - t_K$. If $\mathcal{P}(\chi^2)$ of the fits for both the single- and double-pulse hypotheses was less than 5×10^{-5} in any of the kaon fibers, then the event was rejected. In addition, the fitted time of the first pulse (t_1) was required to be consistent with average time of the kaon fibers. If any kaon fiber failed the requirement $-6 < t_1 - t_K < 7$ ns, then the event was rejected. This requirement was made on the fitted time t_1 of the single-pulse hypotheses if the probability of χ^2 was greater than 25% and on the fitted time t_1 from the double-pulse hypothesis otherwise. The requirement on t_1 rejected events in which the CCD fitter attempted to fit a fluctuation in the tail of the reference pulse to the data pulse or when there was a large second pulse in the fiber being fit and the fitter mistakenly identified it as the first pulse. For events passing these criteria, the second-pulse activity in a K^+ fiber as found by the target CCD fitting was required to be below 1.25 MeV when the fitted second-pulse time t_2 satisfied the coincidence condition $-7.5 \leq t_2 - t_\pi \leq 10$ ns. An example of the fit for a high gain CCD target element is shown in Figure 8. In the following we refer to these requirements on the CCD pulse fitting as the "CCDPUL" cut.

Kaon fiber timing

The target K^+ fiber hits were required to be consistent with a kaon approaching the K^+ decay vertex. This consistency was checked by tabulating the times of the kaon fiber hits against the distance to the decay vertex in the x-y plane and against the range of the kaon as determined by deposited energy. This requirement removed events in which the kaon decay vertex was incorrectly assigned.

Pion fiber energy

Pion fibers were required to have energies less than 3.0 MeV. This suppressed π^+ target-scatters since the expected mean energy deposited in a π^+ fiber was approximately 1.2 MeV.

The deposited energy assigned to the pion in the target was required to be consistent with that expected for a π^+ using a cut on a likelihood function. The likelihood function was created based on the measured range and
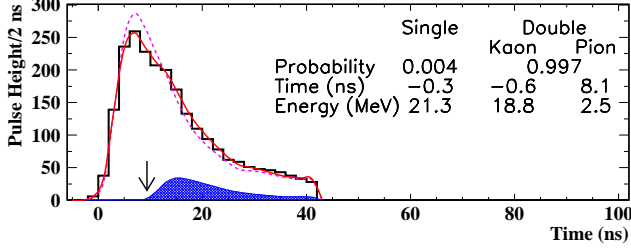
FIG. 8: CCD pulse fit example. The histogram represents the pulse height distribution for the high gain CCD data. The histogram was terminated at 42 ns due to a software cutoff. The dashed (solid) line represents the fitted total pulse height distribution of the single-(double-)pulse hypothesis. The filled area represents the pulse height distribution of the fitted second pulse for the double-pulse hypothesis. The arrow indicates t_{RS}, the expected time of the second pulse based on the reconstructed π^+ in the range stack. The probability, time in ns and energy in MeV of the two fit hypotheses are given in the figure. This event was rejected because the 2.5 MeV of the fitted second pulse was coincident with t_{RS}.

energy of the pion in the target and the pion momentum and calibrated using π_{scat} monitor trigger events. In addition, we required that the total energy of the π^+ target fibers be in the range of 1 to 28 MeV and that the total energy within ± 5.0 ns of t_{rs} in the target edge fibers be less than 4.0 MeV.

Pattern of kaon and pion fibers

Events with a minimum distance between the closest pair of kaon and pion fibers greater than 0.6 cm, more than one fiber width, were rejected. This cut suppressed the CEX background. A more stringent version of this cut that also required that no γ fibers filled the gap between the kaon and pion fibers was developed to define the normalization branches for the CEX (Section III C 3) and two-beam (Section III C 5) background measurements.

Two conditions were used to enforce consistency between the positions of the target kaon decay vertex, the kaon and pion clusters, and the beam particle in the B4 hodoscope. The first condition required that the distance in the xy-plane between the hit position in the B4 hodoscope and the nearest tip of the kaon fiber cluster be less than 1.8 cm. The kaon cluster tips were defined to be the two kaon fibers farthest apart from each other (Figure 6). The second condition required that the distance in the xy-plane between the kaon decay vertex and the nearest kaon cluster tip was less than 0.7 cm. This requirement suppressed $K_{\pi 2}$ target-scatter background when the scattered π^+ did not emerge from the fiber containing the K^+ decay.

The total energy in the target opposite-side pion fibers within 4.0 ns of t_π was required to be less than 1.0 MeV to suppress background due to K_{e4} decays as well as $K_{\pi 2}$

scatters. In the following Sections, this cut is referred to as "OPSVETO".

Target-track fitter

The track determined by the target-track fitter was required to be consistent with the information in the target fibers and the fitted UTC track in order to suppress backgrounds due to pion scattering, CEX, K_{e4} or a second beam particle in the target. For three components χ_5^2, χ_6^2 and χ_7^2 of the χ^2 for the least-squares fit, we required the probability of χ^2 ($\mathcal{P}(\chi_5^2 + \chi_6^2 + \chi_7^2)$) to be greater than 1%. These components were defined as follows:

- χ_5^2 was assigned a contribution for each pion fiber traversed by the track based on the comparison of the observed energy with the expected energy from the calculated range of the track and the track momentum.

- χ_6^2 was assigned a contribution based on the minimum distance between the track and the nearest point of each fiber that was traversed by the track, but had no observed energy. This assignment acted to force the fitted track to go between fibers and thus provided precise position information on the track.

- χ_7^2 was assigned a contribution for pion fibers that were not traversed by the fitted track based on the distance to the nearest corner.

We rejected events if any single pion fiber contributed more than 35 units to χ_5^2 which might indicate a pion scatter in that fiber. We also required the fitted target track to intersect the kaon vertex fiber. The angle between the reconstructed target track and the UTC track was required to be less than 0.01 radian when the range of the π^+ in the target was less than 2.0 cm. In addition the position of the reconstructed π^+ trajectories from the target and UTC fits were required to be well-matched at the target edge. Kinks in the target π^+ track were suppressed by requiring that the difference in the distance of the farthest and nearest pion fiber to the center of the fitted helix of the UTC track was less than 0.35 times the pion range in the target.

3. Pion track requirements

Good pion track reconstruction was required based on the χ^2 of UTC track fit. The cut on the χ^2 was dependent on the number of anode and cathode hits assigned to the fitted track as well as on the number of unused anode and cathode hits. The criteria were determined using both π_{scat} and $K_{\pi 2}$ monitor trigger data such that the π^+ momentum resolution of 2.3 MeV/c for the $K_{\pi 2}$ peak [2] was not degraded.

Additional range-stack quality cuts were placed on the probability of χ^2 of the range-stack track fit and the agreement of the z position of the extrapolated UTC track with the range-stack timing information and, when applicable, the RSSC information. The RSSC was not

available for charged pions that stopped in range stack layers 6 through 10 in contrast to the $\pi\nu\bar{\nu}(1)$ analysis [2].
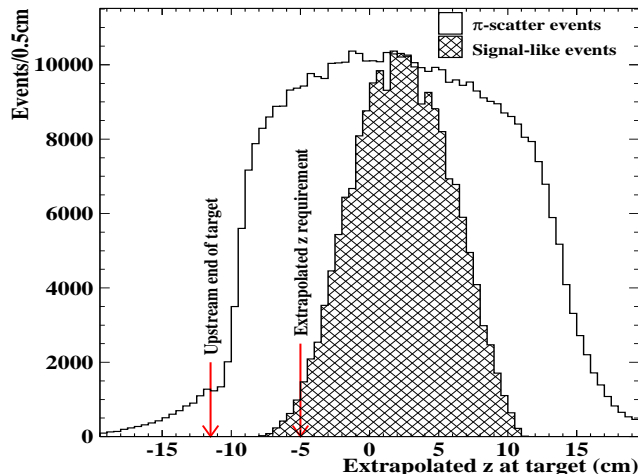

FIG. 9: Extrapolated target z distribution of the charged track. The "π-scatter" and "signal-like" events are taken from π_{scat} and $K_{\mu 2}$ monitor trigger data, respectively. The minimum requirement on the extrapolated z and the upstream end of the target are shown in the figure.

Kaons that come to rest in the target were required to have energy loss in the B4 hodoscope and the target consistent with the measured K^+ stopping position based on the z position of the extrapolated UTC track. A likelihood function was formed based on these three quantities and calibrated using $K_{\mu 2}$ monitor trigger data. The requirement on this "Beam Likelihood" function suppressed $K_{\pi 2}$ target-scatter and CEX backgrounds as well as background due to an incoming beam pion that scattered in the target. In addition we required the z of the extrapolated track to be greater than 6.5 cm from the upstream end of the target. The z distribution of the extrapolated charged track in the target is shown in Figure 9.

4. Decay pion kinematic requirements

The total range (energy) of the π^+ track was calculated as the sum of the measured range (energy) in the target, IC and range stack. The total momentum was obtained from the curvature of the fitted track in the UTC after adjustments due to energy loss in the target and IC. Tiny corrections are applied to R_π, E_π and P_π to take into account the inactive material in the UTC [2].

The upper limit of the signal region in range, energy and momentum was increased with respect to the previous $\pi\nu\bar{\nu}(2)$ analyses [35, 43] to be approximately 2.5 standard deviations from the $K_{\pi 2}$ peak similar to the approach used for the E949 $\pi\nu\bar{\nu}(1)$ analysis [2]. The lower limits were not changed with respect to the pre-

vious $\pi\nu\bar{\nu}(2)$ analyses. The standard signal region was $140 < P_\pi < 199$ MeV/c, $60 < E_\pi < 100.5$ MeV and $12 < R_\pi < 28$ cm.

A tighter kinematic region was defined as a subset of the standard region to further suppress $K_{\pi 2}$ and K_{e4} backgrounds. As shown in Figure 14, $K_{\pi 2}$ and K_{e4} events were not uniformly distributed in the signal region. The $K_{\pi 2}$ target-scatter events were uniformly distributed in the signal region except for a tail near the $K_{\pi 2}$ peak. The imposition of the trigger on the K_{e4} momentum distribution shown in Figure 1 caused the K_{e4} background to peaked around 160 MeV/c as described in Section III C 2. The accepted $K^+ \to \pi^+ \nu\bar{\nu}$ spectrum was monotonically increasing with momentum in the signal region. Based on these observations, the kinematic region that maximized the signal acceptance while minimizing the total $K_{\pi 2}$ and K_{e4} background was $165 < P_\pi < 197$ MeV/c, $72 < E_\pi < 100$ MeV and $17 < R_\pi < 28$ cm.

We also defined the "$K_{\pi 2}$-peak" by the requirements $199 < P_\pi < 215$ MeV/c, $100.5 < E_\pi < 115$ MeV and $28 < R_\pi < 35$ cm. Events in the $K_{\pi 2}$-peak were employed to set selection criteria, estimate background and determine the signal acceptance.

5. Photon veto requirements

Photon veto requirements were fulfilled within a sub-detector when the sum of activity occurring within a time window exceeded an energy threshold. The time window was referenced to t_{RS}, the reconstructed time of the pion in the range stack. The time window and energy threshold was set for the BV, BVL, range stack, EC, EC$_{inner}$ (the inner ring of the upstream EC was considered a separate sub-detector as it had higher accidental rates than the remaining EC elements due to its proximity to the incoming beam), EC$_{2nd}$ (EC energy identified by a double-pulse-finding algorithm using CCD information was treated as a separate sub-detector), target, IC, VC, CO, and μCO by an optimization algorithm described in [2]. The optimization procedure determined the rejection and acceptance as the time window and energy threshold were varied. The optimization goal was to maximize rejection for a given value of acceptance. The acceptance sample used by the optimization procedure was derived from $K_{\mu 2}$ monitor trigger data.

The photon veto requirements for the $\pi\nu\bar{\nu}(1)$ analysis were optimized using the rejection of $K_{\pi 2}$ peak events that were the dominant background with photons in the final state. Ideally the $\pi\nu\bar{\nu}(2)$ photon veto requirements would have optimized the rejection on a sample of $K_{\pi 2}$ target-scatter events; however, given that photon veto rejection needed to be $\mathcal{O}(2500)$, we were unable to prepare such a sample with sufficient statistics, $\mathcal{O}(250000)$ events, needed to avoid biasing the optimization result. In lieu of this sample, we optimized the photon veto requirements for a majority of sub-detectors using a sample of $K_{\pi 2}$ peak events and then optimized the requirements

for the remaining sub-detectors using multiple samples of $K_{\pi 2}$ target-scatter events as described below.

One sample, dubbed the "kink" sample, contained $K_{\pi 2}$ target scatters where the π^+ track had an identifiable kink in the $x-y$ projection, and was created by processing every $\pi\nu\bar{\nu}(1+2)$ event with a target-track reconstruction algorithm which differed from the target-track reconstruction used for signal candidates (Section III B 1). For kink reconstruction, the restrictions on the pion fiber energy were removed as well as the requirement that the pion fibers had to lie within 1 cm of the extrapolated UTC track. The following criteria defined a valid kink event: (1) the event had at least two pion fibers that deviated from the UTC extrapolation, (2) at least one of the fibers from (1) must be adjacent to a kaon fiber, (3) the remaining fibers must be conjoined in a relatively straight line and (4) the event must be rejected by the criteria placed on the standard target-track reconstruction. The final criterion guaranteed that the kink sample was independent of the sample of signal events. Although the resulting kink sample had only 12000 events, it provided a sample rich in target scatters that was used in understanding the response of the AD as described below.

The main sample of $K_{\pi 2}$ target-scatter events was composed of events that failed either the CCDPUL cut (Section III B 2) or the Beam Likelihood cut (Section III B 3) and contained 26317 (52621) events in the 1/3 (2/3) data sample. Additional $K_{\pi 2}$ target-scatter samples were composed of events failing these cuts or the other target cuts described in Section III B 2. The size of the additional samples ranged from 11037 (22037) to 29899 (59871) in the 1/3 (2/3) data samples. While these samples were not completely independent of one another, they contained different relative populations of π^+ that initially traveled parallel or perpendicular to the beam direction before scattering.

Before beginning the optimization procedure, we applied a cut on the activity in the BV prior to t_{RS} (BV_{early}) because we found that a large energy deposit (> 30 MeV) in the BV prior to the kaon decay would prevent the TDCs from registering activity coincident with t_{RS} [44]. The $\pi\nu\bar{\nu}(1)$ set of parameters as listed in Table VI of [2] was the starting point for the $\pi\nu\bar{\nu}(2)$ optimization that included all sub-detectors except the AD and DPV. A primary and secondary set of parameters were determined for the eleven sub-detectors listed in Table I.

The AD parameters were determined using the kink sample after application of a photon veto with a rejection of approximately 175 with looser settings on the parameters of the other sub-detectors. These AD parameters yielded an additional photon veto rejection of 1.95 ± 0.08 with a 94% acceptance factor [44]. The primary $K_{\pi 2}$ target-scatter sample described above was used to optimize the DPV parameters. After application of all other photon veto parameters at the primary setting listed in Table I, the DPV rejection was measured to be 1.13 ± 0.09 with an acceptance factor of 99.99%.

TABLE I: Time window and energy threshold of the primary and secondary photon veto requirements for each sub-detector as described in the text. The time window was defined with respect to t_{RS}, the reconstructed time of the π^+ in the range stack. RS and TG label the range stack and target parameters, respectively. The parameters for the sub-detectors below the double line were optimized separately. BVL_{early} had the additional requirement that reconstructed z position satisfy $|z| < 4$ cm.

| | Primary | | Secondary | |
Sub-detector	Time window (ns)	Threshold (MeV)	Time window (ns)	Threshold (MeV)
BV	[-5.7,10.2]	0.2	[-7.5,10.2]	0.7
BVL	[-4.4,10.7]	0.3	[-3.5,10.6]	0.3
RS	[-4.3,4.4]	0.3	[-3.3,7.8]	0.6
EC	[-4.4,8.0]	0.4	[-6.0,9.5]	0.2
EC_{inner}	[-3.7,5.6]	0.2	[-14.0,9.1]	0.2
EC_{2nd}	[-5.7,2.5]	10.6	[-5.7,2.7]	0.2
TG	[-2.7,2.2]	2.0	[-6.6,2.3]	1.7
IC	[-2.0,4.5]	5.0	[-2.9,9.3]	1.4
VC	[-6.6,1.8]	6.8	[-7.5,7.1]	5.0
CO	[-0.1,5.9]	0.6	[-0.8,5.1]	6.0
μCO	[-5.5,2.3]	3.0	[-4.5,3.3]	1.6
BV_{early}	[-35.7,-5.7]	30.0	[-37.5,-7.5]	30.0
AD	[-2.0,8.0]	0.6	[-2.0,8.0]	0.6
DPV	[-5.0,10.0]	0.0	[-5.0,10.0]	0.0
BVL_{early}	[-5.0,-2.0]	10.0	[-5.0,-2.0]	10.0

The BVL_{early} cut was devised as a "safety" cut subsequent to the single-cut failure study on the 1/3 sample (Section III C 9). The cut removed potential $K_{\pi 2}$ background when both photons from the π^0 decay deposited energy in the same BVL element. Such an occurrence yielded a reconstructed time earlier than t_{RS}, a reconstructed z position near the center of the element and an apparent energy greater than 10 MeV.

Figure 10 shows the offline rejection for fixed values of of the total (online and offline) acceptance for the photon veto. The parameters in the primary column in Table I corresponded to the standard photon veto ("Standard" in the Figure). For the more restrictive ("Tight") photon veto cut described in Section III E, the AND of the parameters in the primary and secondary columns were applied. The additional settings labeled "Loose" and "$\pi\nu\bar{\nu}(1)$" in the Figure, of the photon veto cuts were used for background estimation (Section III C 4) and consistency checks (Section III C 8).

6. Delayed coincidence requirements

Determining that the incoming K^+ came to rest in the target was accomplished by observing the delay between the outgoing charged track and the incoming particle. This requirement rejected incoming beam pions that scattered in the target as well as the products of
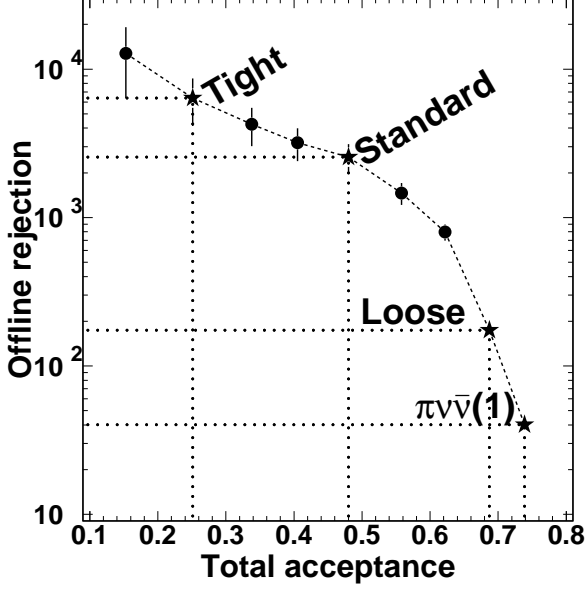
FIG. 10: The offline rejection *vs.* total acceptance for the photon veto. The error bars represent the statistical uncertainty. The labeled starred points are described in the text.

K^+ decay-in-flight. The delayed coincidence also served to suppress the CEX background.

For the standard delayed coincidence requirement, the average time of the kaon fiber hits (t_K) had to be at least 3 ns earlier than the average time of the pion fiber hits (t_π). The previous $\pi\nu\bar{\nu}(2)$ analyses [35, 43] used a tighter requirement of $t_\pi - t_K > 6$ ns. The looser requirement in this analysis resulted in a 9% relative acceptance increase. Under certain conditions the resolution on t_K or t_π was degraded, the degraded time resolution was taken into account by increasing the minimum delayed coincidence allowed. It was increased to 4 ns when the energy deposit in the target kaon fibers was less than 50 MeV, when the time of any of the individual kaon fiber differed from the average kaon fiber time by more than 2 ns or when the time of an individual target pion fiber differed from the average time of the pion fiber hits by more than 3.5 ns. It was increased to 5 ns when the difference between t_K and the B4 hodoscope hit time was greater than 1 ns or when t_π was determined using IC hit time because the average time of the pion fiber hits had poor resolution. It was increased to 6 ns when the difference between t_π and t_{RS} was greater than 1.5 ns.

A tight version of the delayed coincidence with the requirement that $t_\pi - t_K > 6$ ns was used to subdivide the signal region as described in Section III E.

7. Muon identification

Muon backgrounds were rejected largely based upon the positive identification of the π^+ in the range stack by the observation of the $\pi \to \mu \to e$ decay chain and by the range-momentum relationship.

The $\pi\nu\bar{\nu}(1)$ identification algorithms [2] were adopted for this analysis, and a only brief description is provided here. The analysis of the waveform provided by the transient digitizers (TDs) was used to identify the $\pi^+ \to \mu^+\nu_\mu$ decay in the range stack element that contained the stopping pion. A neural network with five input variables was trained using kinematically identified π^+ and μ^+ that stopped in the range stack. The $\mu^+ \to e^+\nu_e\bar{\nu}_\mu$ decay was identified by TDC information in the range stack counters near the stopping counter.

Since previous $\pi\nu\bar{\nu}(2)$ analyses [35, 43] had shown that muon backgrounds were small, less restrictive requirements on the $\pi \to \mu \to e$ decay than the $\pi\nu\bar{\nu}(1)$ analysis were used for the standard $\pi\nu\bar{\nu}(2)$ requirements for a 10% increase in signal acceptance. A muon rejection of 133.0 ± 10.7 (Section III C 4) was obtained with a looser requirement on the neural network output and no identification of the $\mu \to e$ decay. The $\pi\nu\bar{\nu}(1)$ requirements were used to define a tighter cut that was used to subdivide the signal region as described in Section III E. The tighter cuts had a muon rejection of 409.1 ± 60.9. In the following we refer to the $\pi \to \mu \to e$ requirements as the "TD" cuts.

The ability to separate pions from muons using the range and momentum measurements can be seen in Figure 4. The separation was based on the "RNGMOM" cut that was placed on the quantity $\chi_{rm} = (R_{RS} - R_{UTC})/\sigma_R$ where R_{UTC} (σ_R) was the expected range (uncertainty in range) for a given π^+ momentum and R_{RS} was the measured range.

C. Evaluation of backgrounds

1. $K_{\pi2}$-related background

The $K_{\pi2}$-related background contained three components: $K_{\pi2}$ target-scatter, $K_{\pi2}$ range-stack-scatter and $K_{\pi2\gamma}$. For a $K_{\pi2}$ event to have appeared in the signal region, the photons from the π^0 decay had to escape detection and the π^+ had to lose energy via scattering or resolution effects such that it fell into the signal phase space. This scattering could happen in the target ($K_{\pi2}$ target-scatter) or in the range stack ($K_{\pi2}$ range-stack-scatter), but the target-scatter component dominated. Since the π^+ from a $K_{\pi2\gamma}$ decay was not monochromatic, the three final-state photons needed to escape detection for this type of event to be a background.

The topology of the most problematic type of $K_{\pi2}$ target-scatter was that of a π^+ initially traveling along the same target fibers in which the kaon deposited energy and scattering into the active region of the detector
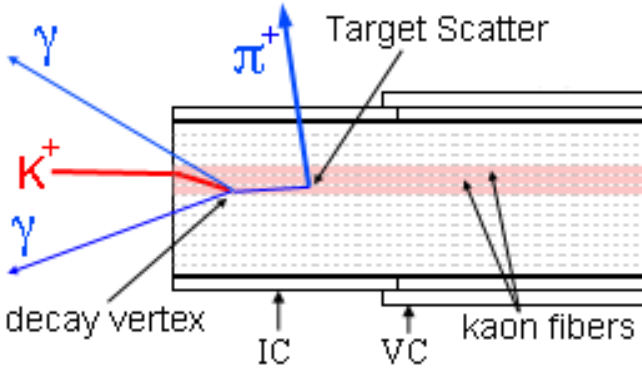
FIG. 11: Schematic representation of a $K_{\pi 2}$ target-scatter in which the π^+ initially traveled in the z direction, scattered in a kaon fiber and was directed into the barrel region. The two photons from the decay of the recoiling π^0 were directed into the endcap region.

as indicated schematically in Figure 11. This type of target-scatter was difficult to reject because some energy deposited in the target by the scattering π^+ occurred in a kaon fiber (Section III B 2) and could not be distinguished from the larger energy deposited by the stopping kaon. In addition this type of target-scatter was difficult to reject because of the back-to-back production of the π^+ and π^0. A π^+ initially traveling along the kaon fibers meant that the π^0 was also traveling parallel to the beam direction and the resulting photons from the π^0 decay were directed at the upstream or downstream ends of the detector where the photon veto was weak.

In the $K_{\pi 2}$ target-scatter background study, the two bifurcation cuts were chosen as the Standard photon veto cuts (CUT1) and the target-quality cuts (CUT2) since both of these could give powerful rejection of the $K_{\pi 2}$ target-scatter background. The bifurcation analysis sample was prepared by applying cuts to remove the contamination from muon, beam and charge exchange events. In the normalization branch, a combination of $K_{\pi 2}$ target-scatter, $K_{\pi 2}$ range-stack-scatter and $K_{\pi 2\gamma}$ events were selected by inverting the photon veto cut ($\overline{\text{CUT1}}$). All target quality cuts (CUT2) were applied to the sample, resulting in 1131 events left in the normalization branch. After corrections (detailed below) for $K_{\pi 2}$ range-stack-scatter contamination, $N_{\text{norm}} = 1107.7 \pm 33.8(\text{stat.})^{+2.9}_{-2.8}(\text{syst.})$ events remained in the normalization branch. The systematic uncertainty comes from the systematic uncertainty of the range-stack-scatter cuts when correcting the $K_{\pi 2}$ normalization branch for $K_{\pi 2}$ range-stack-scatter contamination. Corrections for contamination due to $K_{\pi 2\gamma}$ contamination are discussed later in this Section.

For the $K_{\pi 2}$ target-scatter rejection branch, the $K_{\pi 2}$ target-scatters were classified into two non-exclusive categories. The first category, known as "z-scatters", occurred when the π^+ traveled parallel or anti-parallel to the beam direction, scattered in a kaon fiber and into

the active region of the detector as depicted in Figure 11. The second category, known as "xy-scatters", occurred when the π^+ scattered outside of the kaon fibers and the scatter was visible in the xy-plane. To measure the rejection of the photon veto for target-scatter events, six classes of $K_{\pi 2}$ target-scatter events were created by applying or inverting various combinations of the requirements on π^+ in the target (Section III B 2) creating samples with varying mixtures of xy-scatter and z-scatter events. The primary $K_{\pi 2}$ target-scatter sample (Section III B 5) was considered to be the richest in z-scatters and was chosen to measure the photon veto rejection, giving 52 621 events for the region C + D. The photon veto cuts (CUT1) were then applied to the remaining $K_{\pi 2}$ target-scatter events, leaving 22 events for the region C. The pion momentum distributions of the normalization and rejection branches are shown in Figure 12. The photon veto rejection of the other five classes of target-scatter events was also measured as well as the photon veto rejection of the main $K_{\pi 2}$ target-scatter sample in the tighter kinematic region (Section III B 4). The range of measured rejection values was used to set the systematic uncertainty in the photon veto rejection on the $K_{\pi 2}$ target-scatters, giving a photon veto rejection of $52621/22 = 2392 \pm 510^{+366}_{-188}$. The uncorrected $K_{\pi 2}$ target-scatter background was measured to be

$$
\begin{aligned}
b_{\text{un}}^{tg} &= 3/2 \times (1107.7 \pm 33.8^{+2.9}_{-2.8})/(2392 \pm 510^{+366}_{-188} - 1) \\
&= 0.695 \pm 0.150^{+0.067}_{-0.100}, \quad\quad (4)
\end{aligned}
$$

where the first uncertainty was statistical and the second uncertainty systematic. The correction to the $K_{\pi 2}$ target-scatter background due to $K_{\pi 2\gamma}$ is described below.

For the $K_{\pi 2}$ range-stack-scatter background events, the cuts with the most powerful rejection were the range-stack quality cuts and the photon veto. The $K_{\pi 2}$ range-stack-scatter normalization branch was a modified version of the $K_{\pi 2}$ target-scatter normalization branch, with the range-stack quality cuts inverted instead of being applied before the inversion the photon veto cut as was done in the $K_{\pi 2}$ target-scatter normalization branch. This sample of $N_2 = 281$ events was heavily contaminated with target-scatter events due to the inefficiency of the range-stack-scatter cuts. The $N_1 = 1131$ events remaining at the end of the $K_{\pi 2}$ target-scatter normalization branch consisted of N^{tg} $K_{\pi 2}$ target-scatter events with contamination due to N^{rs} range-stack-scatter events:

$$
N^{tg} + N^{rs} = N_1. \quad\quad (5)
$$

These N^{tg} $K_{\pi 2}$ target-scatter events and N^{rs} $K_{\pi 2}$ range-stack-scatter events were also related to the N_2 events remaining in the $K_{\pi 2}$ range-stack-scatter normalization branch by

$$
\frac{1-A}{A} \times N^{tg} + (R-1) \times N^{rs} = N_2, \quad\quad (6)
$$

where $A = 0.888 \pm 0.001(\text{stat.}) \pm 0.012(\text{syst.})$ was the acceptance factor for the range-stack quality cuts (Sec-
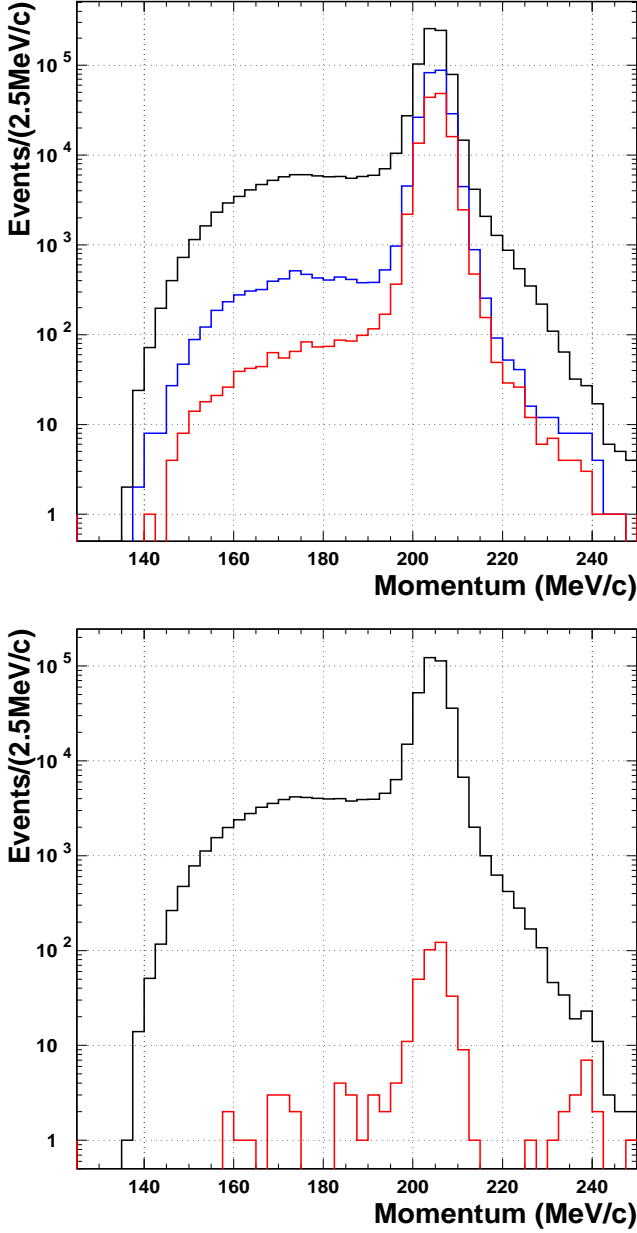
FIG. 12: (Top) Pion momentum distribution for the normalization branch in the 2/3 data sample. The black curve represents the distribution after inversion of the photon veto cut. The blue curve shows the suppression of the all the target cuts except for the CCDPUL cut and the red curve shows the suppression of all the target cuts including the CCDPUL cut. (Bottom) Pion momentum distribution of the rejection branch in the 2/3 data sample. The events obtained from the inversion of the target cuts is shown in black and the red curve shows the events that survive the photon veto. The events surviving the photon veto that peak near 236 MeV/c were due to $K_{\mu 2}$ decays. The cuts on pion kinetic energy and range were not applied for these distributions in order to observe the momentum distribution outside the $\pi\nu\bar{\nu}(2)$ signal region.

tion III D) and $R = 7.06 \pm 0.47$ was the rejection of $K_{\pi 2}$ range-stack-scatter events by the range-stack quality cuts measured using events with momentum consistent with the $K_{\pi 2}$-peak (Section III B 4), but range and energy in the $\pi\nu\bar{\nu}(2)$ signal region as would be expected for a range-stack-scatter. The systematic uncertainty on A was due to the larger uncertainty on the measured kinematics of the π_{scat} monitor data used to measure the acceptance of the range-stack quality cuts as described in Section III D. By solving Equations (5) and (6) simultaneously, it was possible to estimate the number of $K_{\pi 2}$ target-stack events ($N^{tg} = 1107.7 \pm 33.8^{+2.9}_{-2.8}$) and the number of $K_{\pi 2}$ range-stack-scatter events ($N^{rs} = 23.3 \pm 3.5^{+2.9}_{-3.0}$) present in the original $K_{\pi 2}$ target-scatter normalization branch, where the first uncertainty is statistical and the second is systematic due to the acceptance factor A.

The photon veto rejection on the $K_{\pi 2}$ range-stack-scatter events should be the same as that for the unscattered $K_{\pi 2}$ peak events as the back-to-back correlation of the π^+ and π^0 was maintained. The $K_{\pi 2}$ range-stack-scatter rejection branch was created by applying all analysis cuts other than the photon veto cut and the signal kinematic cuts. Instead the $K_{\pi 2}$ peak events were selected, creating a sample of $K_{\pi 2}$ events that did not scatter in the target, giving 122 581 events for the region C + D. The PV cuts (CUT1) were then applied to the remaining $K_{\pi 2}$ events leaving 106 events in region C for a photon veto rejection of $122581/106 = 1156 \pm 112$. The $K_{\pi 2}$ range-stack-scatter background was measured to be

$$
\begin{aligned}
b^{rs} &= 3/2 \times (23.3 \pm 3.5^{+2.9}_{-3.0})/(1156 \pm 112 - 1) \\
&= 0.030 \pm 0.005(\mathrm{stat.}) \pm 0.004(\mathrm{syst.}) \tag{7}
\end{aligned}
$$

The $K_{\pi 2\gamma}$ background estimate did not use the bifurcation method, but instead used a combination of $K_{\pi 2}$ data and simulated $K_{\pi 2}$ and $K_{\pi 2\gamma}$ events. We simulated both the inner bremsstrahlung and direct emission amplitudes of $K_{\pi 2\gamma}$ decays assuming no interference between the amplitudes [45]. The inner bremsstrahlung provided the dominant contribution. The $K_{\pi 2\gamma}$ background was estimated as

$$
b^{\gamma} = \frac{N}{\kappa R_{\gamma}} \tag{8}
$$

where

- $N = 106$ was the number of $K_{\pi 2}$-peak events in the $\pi\nu\bar{\nu}(1+2)$ trigger sample after all selection criteria were applied except that the $K_{\pi 2}$-peak kinematic region was selected.

- $\kappa = 417 \pm 24$ was the ratio of acceptance factors of $K_{\pi 2}$ to $K_{\pi 2\gamma}$ events as determined from simulated $K_{\pi 2}$ and $K_{\pi 2\gamma}$ decays taking into account the $K_{\pi 2}$ and $K_{\pi 2\gamma}$ branching ratios. We used $\mathcal{B}(K^+ \rightarrow \pi^+\pi^0\gamma) = (11.1 \pm 0.6) \times 10^{-4}$ obtained by correcting the partial branching ratio $(2.75 \pm 0.15) \times 10^{-4}$ [25] measured for $55 < P_{\pi} < 90$ MeV to the full energy range using simulation.

$R_\gamma = 5.04 \pm 0.10$ was the additional photon veto rejection afforded by the radiative photon. This additional rejection was calculated by combining the distribution of the radiative photon from simulated events with the measured single photon detection efficiency as a function of angle and energy from $K_{\pi2}$ data [46].

The final $K_{\pi2\gamma}$ background estimate was given by

$$b^\gamma = \frac{N}{\kappa \cdot R_\gamma} = 0.076 \pm 0.007 \pm 0.006, \qquad (9)$$

where the first uncertainty was statistical and the second was systematic (due to κ and R_γ).

The inverted photon veto used to select events for the $K_{\pi2}$ target-scatter normalization branch would have also selected $K_{\pi2\gamma}$ events. We assumed that initial estimate of the $K_{\pi2}$ target-scatter background also contained the contribution from $K_{\pi2\gamma}$. We therefore corrected the estimate for the $K_{\pi2}$ target-scatter background by subtracting b^γ so that the final, corrected $K_{\pi2}$ target-scatter background estimate was

$$
\begin{aligned}
b^{tg} &= b^{tg}_{un} - b^\gamma \\
&= 0.695 \pm 0.150^{+0.067}_{-0.100} - 0.076 \pm 0.007 \pm 0.006 \\
&= 0.619 \pm 0.150^{+0.067}_{-0.100} \quad . \qquad (10)
\end{aligned}
$$

2. K_{e4} background

Despite the small $K^+ \rightarrow \pi^+\pi^-e^+\nu$ branching ratio of $(4.09 \pm 0.10) \times 10^{-5}$ [25], K_{e4} could be a background if the π^- and the e^+ escaped detection in the target. The low energy distribution of the total kinetic energy of the π^- and the e^+ vs. the reconstructed π^+ momentum in simulated events shown in Figure 13 indicates where the K_{e4} background would occur kinematically.

Since the main characteristic of K_{e4} event was extra energy in the target from the π^- and the e^+, the target photon veto (TGPV), OPSVETO and CCDPUL cuts were the most effective cuts to suppress this background. Due to contamination by other types of background, such as $K_{\pi2}$-target-scatter, it was not possible to isolate a pure K_{e4} background sample for a bifurcation analysis using data only. Nonetheless, a K_{e4}-rich sample was selected from data using the CCDPUL $\cdot$ $\overline{\text{TGPV} \cdot \text{OPSVETO}}$ requirement and served as the normalization branch. We established that the majority of the events in the normalization branch were likely to be due to K_{e4} decays by removing the CCDPUL requirement and comparing the momentum distribution of the selected events in the 1/3 sample with the expectation from simulation (Figure 14). In addition, these events were visually examined and determined to be largely due to K_{e4} decays with some contamination from $K_{\pi2}$ at the 10% level. One striking example of a K_{e4} candidate event is shown in Figure 6.
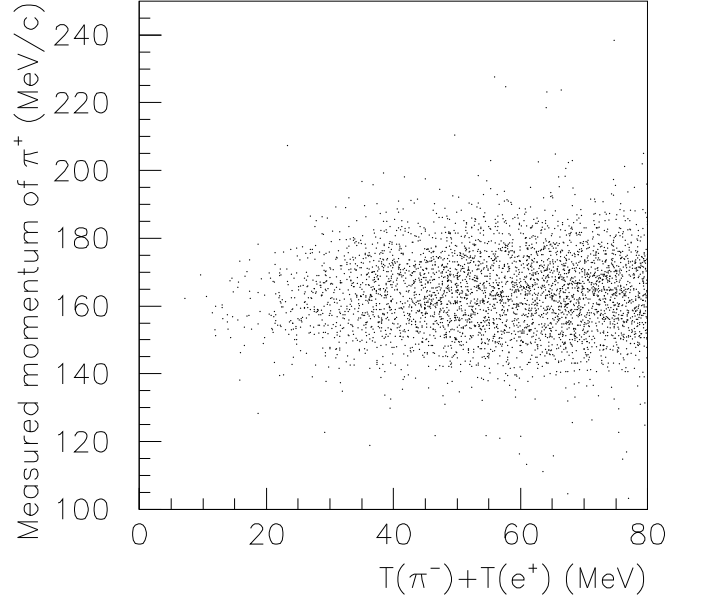

FIG. 13: The sum of the π^- and e^+ kinetic energy versus the measured momentum of the π^+ for simulated K_{e4} events that passed the trigger.
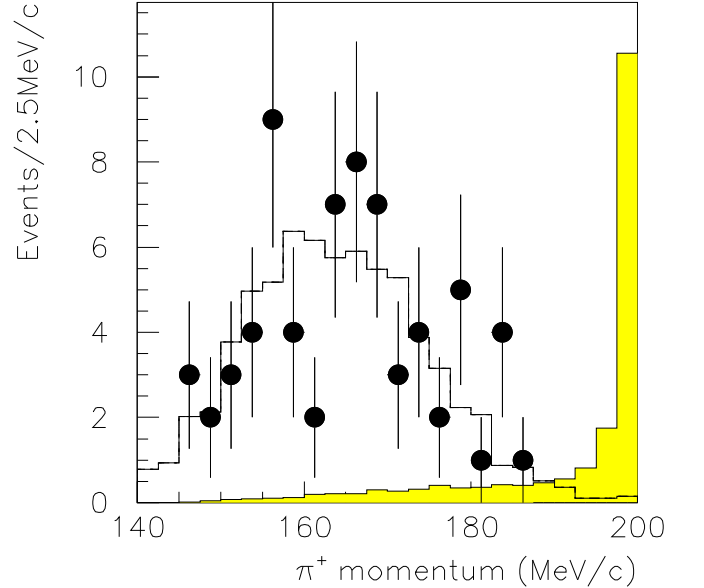
FIG. 14: Momentum distribution of the π^+ in the K_{e4} normalization branch for the 1/3 sample before the application of the CCDPUL cut. The points with error bars represent the data. The unshaded histogram is the distribution as expected from simulated K_{e4} events. The histogram area is normalized to the number of data events. The shaded histogram represents the normalization branch for $K_{\pi2}$ target-scatter events. The ratio of the area of the shaded to the unshaded histogram has been set to 1/8 times the ratio of the $K_{\pi2}$ target-scatter background to the K_{e4} background for display purposes.

Simulated K_{e4} events were used to determine the rejection of the TGPV, OPSVETO, and CCDPUL requirements. Negative pion absorption in the target was modeled based on the energy spectrum of stopped π^- in plastic scintillator observed in E787 [47]. We assumed that all energy generated from π^- absorption would be promptly deposited in the single fiber where the π^- came to rest. This assumption conservatively neglected the possibility that detectable activity from π^- absorption could occur elsewhere in the detector. Positron interactions were well-model-led in our EGS4-based simulation [48]. The rejection of the CCDPUL, TGPV and OPSVETO requirements were correlated because the target fibers containing the deposited energy of the π^- and e^+ could have been classified as kaon, pion, gamma or opposite-side pion fibers. We used the energy of the simulated deposits to estimate the rejection of these cuts as $R = 52^{+121}_{-29}$. As we did not precisely model either π^- absorption or the inactive material of the the target such as the gaps between the fibers and the cladding and wrapping material of each fiber, we varied the threshold for the energy treated by the CCDPUL (TGPV·OPSVETO) cut by a factor of 5 (1.5) to estimate the systematic uncertainty associated with the rejection of these cuts. The normalization branch in the 2/3 sample contained 6 events so the K_{e4} background was measured to be $3/2 \times 6/(52^{+121}_{-29} - 1) = 0.176 \pm 0.072^{+0.233}_{-0.124}$ where the first error was statistical and the second was systematic.

3. Charge exchange background

Interaction of the incident K^+ in the target was a potential source of background. At low energy, pion production from K^+-nucleon scattering was negligible; however, the charge exchange process (CEX) interaction $K^+ n \rightarrow K^0 p$ could contribute background if the recoil nucleus or proton was not detectable.

When the K^0 decayed as a K^0_S or K^0_L it was a potential background. The delayed coincidence requirement effectively removed any contribution from the short-lived K^0_S. The semileptonic decay processes $K^0_L \rightarrow \pi^+ e^- \nu_e$ and $K^0_L \rightarrow \pi^+ \mu^- \nu_\mu$ with branching ratios of 20% and 14%, respectively, were considered to be the most likely to form a background.

We also considered the possibility of background due to hyperon production where a π^+ was either produced with the hyperon or was a hyperon decay product. Hyperon production would result from $\overline{K^0}$-nucleon interactions if the K^0 oscillated to a $\overline{K^0}$.

Simulation studies showed that there was often a gap between the pion and kaon fibers and that the reconstructed z of the pion track was not consistent with the energy deposited in the kaon fibers as indicated schematically in Figure 15. A CEX-rich sample that served as the normalization branch was selected in $\pi\nu\bar{\nu}(1+2)$ triggers by requiring a gap between the pion and kaon fibers. No target energy cuts were applied in the selection of the
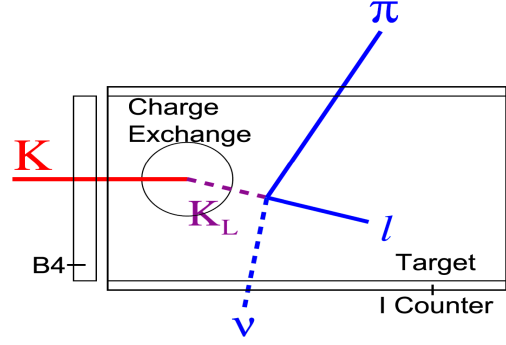

FIG. 15: Schematic diagram of the charge exchange process in the target.

normalization sample since the lepton from K^0_L decay or the π^- and π^0 associated with hyperon production might deposit extra energy in target. The delayed coincidence requirement was also not applied for the normalization sample. In contrast to the previous $\pi\nu\bar{\nu}(2)$ analysis [43], the ability to create a normalization sample from $\pi\nu\bar{\nu}(1+2)$ data avoided uncertainties associated with the effective CEX cross-section and related efficiencies. The rejection associated with finding a gap in the CEX events, the target energy cuts and the delayed coincidence was determined from simulated CEX events. For the simulation of CEX events, we used reconstructed $K^0_S \rightarrow \pi^+\pi^-$ events obtained from the CEX monitor trigger data (Section II B). The reconstructed K^0_S position and momentum vector were used as the K^0_L production point and momentum. The background was measured in the 2/3 sample to be $0.013 \pm 0.013(\text{stat.})^{+0.010}_{-0.003}(\text{syst.})$ The systematic uncertainty was estimated by varying the threshold of the target energy cuts analogous to that for K_{e4} (Section III C 2).

4. Muon background

The decays $K^+ \rightarrow \mu^+ \nu_\mu$, $K^+ \rightarrow \mu^+ \nu_\mu \gamma$ and $K^+ \rightarrow \mu^+ \pi^0 \nu_\mu$ could contribute background in the $\pi\nu\bar{\nu}(2)$ kinematic region as indicated in Figure 4. The latter two decays would be background if the photons went undetected and the first decay would be background if the kinematics of the μ^+ were mis-reconstructed. All three processes also required the muon to be mis-identified as a pion in order to be a background.

The two bifurcation cuts were the $\pi \rightarrow \mu \rightarrow e$ identification or "TD" cut (CUT1) and the π/μ range-momentum separation (CUT2). The normalization branch defined by inverting the TD cut yielded zero events in the 2/3 sample, so N_{norm} was assigned to be 1 event.

The μ^+ rejection branch contained $C + D = 20488$ events in the 2/3 sample and was selected by inverting CUT2 and applying cuts to remove beam backgrounds

and the $\pi\nu\bar{\nu}(1)$ version of the photon veto cut (Figure 10) to suppress $K_{\pi2}$ backgrounds. After the application of the TD cut, the number of events remaining were $C = 154$ for a measured TD cut rejection of 133.0 ± 10.7. Thus, the μ^+ background was estimated to be $3/2 \times 1 \pm 1/(133 - 1) = 0.0114 \pm 0.0114$.

5. Beam background

Besides the charge-exchange background discussed in Section III C 3, beam-related background had contributions from a single entering beam particle and two beam particles.

Single-beam background

The bifurcation cuts for single beam background were the delayed coincidence (CUT1) and B4 energy of less than 1.0 MeV (CUT2), which selects beam pions. The sample was selected by applying all the photon veto cuts except TGPV, the kinematic cuts, TD cuts, beam cuts except delayed coincidence, and CUT2. The rejection sample contained $C + D = 12850$ events in the 2/3 data. After the application of the delayed coincidence $C = 2$ events remained for a rejection of the delayed coincidence cut of 6425 ± 4543. The normalization sample formed by the inversion of the delayed coincidence cut samples yielded zero events, so that N_{norm} was assigned to be 1 ± 1. The measured single beam background was $3/2 \times 1 \pm 1/(6425 - 1) = 0.00023 \pm 0.00023$.

Double-beam background

Double-beam background had two components KK and $K\pi$. For the KK ($K\pi$) background, the decay products of the initial kaon were undetected and a subsequent kaon decay-in-flight (scattered beam pion) provided the outgoing π^+.

The KK component of the double-beam background b^{KK} was determined using the bifurcation procedure described in Section III A 3 with modifications to compensate for poor statistics:

$$b^{KK} = 3/2 \times \frac{n_{KK}/r_{KK}}{R_{KK} - 1} \qquad (11)$$

where the factor of 3/2 was the scale factor for the 2/3 data sample and

$R_{KK} = 1576/4 = 394 \pm 197$ was the measured rejection of the kaon Čerenkov and BWPC cuts (CUT1) on an entering kaon at the time of the outgoing pion (t_{RS}). The rejection sample was prepared by vetoing entering pions at t_{RS} via Čerenkov information, by requiring a second track at t_{RS} in the B4 counter with an energy deposit consistent with a kaon and by the more stringent target gap requirement described in Section III B 2. The latter criterion ensured activity in the target in two spatially and temporally distinct regions indicative of a double-beam event.

$\frac{n_{KK}}{r_{KK}}$ was the normalization provided by a second bifurcation of the standard normalization branch. The second bifurcation exploited the lack of correlation between the AD and target cuts to improve the statistical power of the measurement. The normalization branch was prepared by inverting CUT1, by vetoing entering pions at t_{RS} using Čerenkov information and by application of the $\pi \to \mu \to e$ and track quality requirements on the outgoing track and contained 2699 events. The application of the AD photon veto cuts reduce the sample to 325 events for a rejection of $r_{KK} = 8.3 \pm 0.4$. The application of the target cuts on the 2699 events yielded zero events so we assigned $n_{KK} = 1 \pm 1$.

Inserting these values into Equation (11) gave the KK background of $b^{KK} = 0.00046 \pm 0.00046$.

An analogous method was used to determine the $K\pi$ component of the double-beam background

$$b^{K\pi} = \frac{1}{1 - 0.606} \times 3/2 \times \frac{n_{K\pi}/r_{K\pi}}{R_{K\pi} - 1} \qquad (12)$$

where the additional scale factor was included to correct for the data accumulated with the online pion Čerenkov veto in the $\pi\nu\bar{\nu}(2)$ trigger (Section II B). With the online veto, offline rejection of the pion Čerenkov cuts was low and the normalization branch lacked statistics. We scaled the $K\pi$ background measurement obtained for the data without the online veto by the ratio of the kaon exposures to obtain $b^{K\pi}$. As a check of this scaling, we verified that the KK background measurements for the two trigger configurations were consistent and that the $K\pi$ background for the $\pi\nu\bar{\nu}(1)$ trigger data was consistent for the two data-taking periods [49]. With the measured values of $R_{K\pi} = 2467/4 = 617 \pm 308$, $n_{K\pi} = 1 \pm 1$ and $r_{K\pi} = 4435/464 = 9.6 \pm 0.4$ in Equation (12), we obtained $b^{K\pi} = 0.00064 \pm 0.00064$.

6. Background summary

The contribution of each background component was determined from the 2/3 data sample and listed in Table II. The total background was estimated to be

Process	Background events
$K_{\pi2}$ target-scatter	$0.619 \pm 0.150^{+0.067}_{-0.100}$
$K_{\pi2}$ range-stack-scatter	$0.030 \pm 0.005 \pm 0.004$
$K_{\pi2\gamma}$	$0.076 \pm 0.007 \pm 0.006$
K_{e4}	$0.176 \pm 0.072^{+0.233}_{-0.124}$
Charge-exchange	$0.013 \pm 0.013^{+0.010}_{-0.003}$
Muon	0.011 ± 0.011
Beam	0.001 ± 0.001
Total	$0.927 \pm 0.168^{+0.320}_{-0.237}$

TABLE II: Summary of the estimated number of events in the signal region from each background component. Each component is described in the text.

$0.927 \pm 0.168^{+0.320}_{-0.237}$ events and was dominated by the $K_{\pi 2}$ target-scatter component that also provides the largest contribution to the statistical uncertainty. The systematic uncertainty was dominated by the contribution from the K_{e4} background due to an inability to establish a precise correspondence between the energy observed in the target in data and simulation.

We performed a number of background consistency and validity checks as described below.

7. Background contamination evaluation

Due to the difficulty of isolating background samples, studies were performed to estimate the degree of contamination (i.e., events due to background from other sources) in the $K_{\pi 2}$ target-scatter normalization and rejection branches. In general contamination of the normalization or rejection branch would result in an overestimate of the background.

The effect of muon contamination of the $K_{\pi 2}$ background estimate was determined separately for the normalization and rejection branches with the $\pi \to \mu \to e$ (TD) and π/μ range-momentum separation (RNGMOM) cuts. The normalization branch was assumed to be the sum of π^+ and μ^+ components such that

$$N_{\rm norm} = 1131 = N^{\pi}_{\rm norm} + N^{\mu}_{\rm norm} \quad . \tag{13}$$

When the TD and RNGMOM cuts were not applied, the observed number of events in the normalization branch was

$$n = 12980 = N^{\pi}_{\rm norm}/A_{\pi} + R_{\mu}N^{\mu}_{\rm norm} \tag{14}$$

where A_{π} (R_{μ}) was the acceptance (rejection) factor for the combination of the TD and RNGMOM cuts for pions (muons). The rejection of the TD cut was evaluated as 133.0 ± 10.7 as part of the muon background estimate (Section III C 4). The RNGMOM rejection of 28.3 ± 1.1 was evaluated using the muon normalization branch for a total muon rejection of $R_{\mu} = 3764 \pm 333$. The acceptance factor A_{π} of the combination of the TD and RNGMOM cuts was determined on samples of $K_{\pi 2}$-peak events that failed different combinations of the target-scatter cuts used to assess the uncertainty in the photon veto rejection as described in Section III B 5. The acceptance factors for these samples, both before and after the application of the Standard photon veto cut, were consistent and yielded $A_{\pi} = 0.809 \pm 0.030$. The simultaneous solution to Equations (13) and (14) gave the muon contamination of the normalization sample of $g_{\mu} \equiv N^{\mu}_{\rm norm}/N_{\rm norm} = (2.7 \pm 0.3) \times 10^{-3}$. Analogous methodology was used to assess the effect of muon contamination in the rejection branch. The calculated photon veto rejection after correction for muon contamination was $R^{\pi} = 2410 \pm 518$ to be compared with $R = 2392 \pm 510$ (Section III C 1). Inserting these results into the background estimate using the bifurcation method (Equation (3)) implied that the muon contamination increased the $K_{\pi 2}$ background (b) estimate by

$$
\begin{aligned}
b/b^{\pi} &= f\frac{N_{\rm norm}}{R-1} \Big/ f\frac{N^{\pi}_{\rm norm}}{R^{\pi}-1} \\
&= \frac{1}{1-g_{\mu}}\frac{R^{\pi}-1}{R-1} \\
&= 1.010 \pm 0.002
\end{aligned}
$$

which was considered negligible with respect to the estimated systematic uncertainty.

A similar treatment limited the overestimate of the $K_{\pi 2}$ background due to double-beam contamination to be $< 0.1\%$.

The rejection of K_{e4} by the photon veto should be less than the photon veto rejection of $K_{\pi 2}$ and $K_{\pi 2\gamma}$ in that there were no photons in the final state. Contamination of the $K_{\pi 2}$ rejection sample by K_{e4} events would therefore reduce the measured photon veto rejection. We observed that the measured rejection of $39481/18 = 2193 \pm 517$ in the tighter kinematic region, that was defined to suppress K_{e4} (Section III B 4), was consistent with the overall rejection of 2392 ± 510 (Section III C 1) indicating no significant contamination of the $K_{\pi 2}$ rejection sample by K_{e4}. The $K_{\pi 2}$ normalization branch was defined by the inversion of the photon veto and the application of the target-quality cuts, including CCD-PUL and OPSVETO. The K_{e4} normalization was prepared by application of CCDPUL $\cdot \overline{\text{TGPV} \cdot \text{OPSVETO}}$. Since $\overline{\text{TGPV}} \cdot \text{OPSVETO} \cdot \text{CCDPUL}$ was a subset of the $K_{\pi 2}$ normalization branch, we concluded that the contamination of the $K_{\pi 2}$ normalization branch by K_{e4} was less than the six events selected in the K_{e4} normalization branch (Section III C 2) and hence negligible compared to the 1131 events in the $K_{\pi 2}$ normalization branch (Equation (5)).

8. Background consistency checks

The reliability of the bifurcation method used to estimate the backgrounds relied on the two bifurcation cuts being uncorrelated. Three distinct data regions just outside the signal region were created by loosening the photon veto cut and the CCDPUL cut. For uncorrelated cuts the number of observed events should be consistent with the number of events expected in that region using the bifurcation method. The region CCD_1 was the region immediately adjacent to the signal region defined by increasing the pion energy threshold from 1.25 MeV to 2.5 MeV. The region PV_1 was the region immediately adjacent to the signal region and defined by events rejected by the Standard photon veto and accepted by the Loose photon veto cuts (Figure 10). The region PV_2 was the region adjacent to PV_1 and defined by events rejected by the Loose photon veto and accepted by the $\pi\nu\bar{\nu}(1)$ photon veto cuts (Figure 10).

Table III shows the number of expected and observed events as well as the probability of observation. The com-

Region	N_E	N_O	$\mathcal{P}(N_O; N_E)$	Combined
CCD_1	$0.79^{+0.46}_{-0.51}$	0	0.45 [0.29,0.62]	
PV_1	$9.09^{+1.53}_{-1.32}$	3	0.02 [0.01,0.05]	0.05 [0.02,0.14]
PV_2	$32.4^{+12.3}_{-8.1}$	34	0.61 [0.05,0.98]	0.14 [0.01,0.40]

TABLE III: Comparison of the expected (N_E) and observed (N_O) number of background events in the three regions CCD_1, PV_1, and PV_2 outside the signal region. The central value of N_E is given along with the combined statistical and systematic uncertainties. $\mathcal{P}(N_O; N_E)$ is the probability of observing N_O or fewer events when N_E events are expected. The rightmost column "Combined" gives the probability of the combined observation in that region and the region(s) of the preceding row(s). The numbers in square brackets are the probabilities reevaluated at the upper and lower bounds of the uncertainty on N_E [50].

bined probability of observation of 5% for the two regions nearest the signal region may have indicated that the background was overestimated, but the re-evaluation of this combined probability at the lower limit of the systematic uncertainties [50] gave 14% for the two closest regions which demonstrated that the assigned systematic uncertainties were reasonable.

9. Single-cut failure study

After determination of the selection criteria using the 1/3 data sample, we performed a "single-cut" failure study to identify unexpected sources of background or potential analysis flaws. Individual cuts that exploited similar background characteristics were grouped together to form the following twelve cut categories:

1. The cuts on R_π, P_π and E_π (Section III B 4),

2. All photon veto cuts except those on the AD and target,

3. The photon veto cut on the AD,

4. The target photon veto and OPSVETO (Section III B 2) cut,

5. The delayed coincidence cut (Section III B 6),

6. The pion track requirements (Section III B 3) excluding the cuts in the next two categories and the π/μ range-momentum separation requirement (Section III C 4),

7. The Beam Likelihood cut (Section III B 3),

8. The cut requiring the z position of the extrapolated UTC track to be more than 6.5 cm from the upstream end of the target (Section III B 3),

9. The CCDPUL and kaon fiber timing cuts (Section III B 2),

10. The cuts related to the identification of the $\pi \rightarrow \mu \rightarrow e$ decay chain,

11. The cuts to suppress beam-related backgrounds, and

12. The cuts on pion fiber energy, the pattern of kaon and pion fibers and the target-track fitter (Section III B 2).

All events in the 1/3 data sample that failed only one of these twelve categories were examined. We found four events that contained evidence of two potential analysis flaws.

Three of the events not rejected by the photon veto cuts showed evidence of a large energy deposit in the BVL. These events were shown to be due to $K_{\pi2}$ decays in which both photons from the π^0 decay deposited energy in the same BVL counter [46]. The simultaneous activity at each end of a BVL element led to an erroneous average time prior to t_{RS} that was outside the veto time window. A "safety" cut, previously described in Section III B 5, was devised to remove these events.

The remaining event of the four failed only the photon veto criteria in the AD and revealed a potential flaw in the CCDPUL target-pulse fitting algorithm when the fitted time of the first pulse was inconsistent with the average kaon fiber time. The inconsistency arose when the fitting algorithm incorrectly assigned the first pulse time to an actual second pulse because the second pulse energy was large compared to the first pulse energy. The CCDPUL timing criteria already described in Section III B 2 were developed to remove the analysis flaw.

D. Acceptance and sensitivity

We assessed the acceptance of the selection criteria by dividing the criteria into components that could be measured separately using monitor triggers or simulated data. Simulated data were used to estimate the acceptance of the trigger and decay phase space as well as to assess the impact of nuclear interactions.

1. Acceptance factors from $K_{\mu2}$ events

$K_{\mu2}$ monitor triggers were used to assess the components of the acceptance regarding the kaon beam, the charged track, the event topology and the Standard photon veto. The acceptance factors are listed in Table IV and described below.

To measure the acceptance of the range stack track reconstruction, a sample of $K_{\mu2}$ monitor triggers was selected by requiring a good track in the target and UTC, an energy deposit in the B4 hodoscope consistent with an entering kaon and a delayed-coincidence of > 5 ns based on the $\check{C}_K$ and the IC. The acceptance of the range stack

TABLE IV: Acceptance factors of the $K^+ \to \pi^+ \nu \bar{\nu}$ selection criteria measured with $K_{\mu 2}$ monitor trigger data. Only statistical uncertainties are shown. The product is $A_{K_{\mu 2}}$.

Cut	Acceptance factor
Range stack track reconstruction	0.99993 ± 0.00001
UTC-range stack track matching	0.99943 ± 0.00002
Beam and target pattern	0.15081 ± 0.00018
Photon veto	0.48122 ± 0.00200
$A_{K_{\mu 2}}$	0.07253 ± 0.00031

TABLE V: Acceptance factors measured with $K_{\pi 2}$ monitor trigger data. Uncertainties are statistical only. The product of all factors is $A_{K_{\pi 2}}$.

Cut	Acceptance factor
UTC reconstruction	0.94345 ± 0.00019
OPSVETO	0.97417 ± 0.00063
π^+ identification in target	0.71851 ± 0.00181
$A_{K_{\pi 2}}$	0.6604 ± 0.0018

tracking cuts on the surviving $K_{\mu 2}$ events is given in second row of Table IV.

The acceptance of consistency of the range stack and UTC track was assessed using a $K_{\mu 2}$ sample with a good track in the range stack, a delayed-coincidence of > 5 ns based on the $\check{C}_K$ and the IC, and a single entering kaon selected based on the B4 energy deposit and the beam Čerenkov and wire chambers. The UTC-range stack track matching acceptance factor is given in the third row of Table IV.

The acceptance factor associated with the beam and target pattern recognition was evaluated on a sample of $K_{\mu 2}$ events that were required to have a single entering kaon and a good track in the UTC and range stack with $|\cos \theta| < 0.5$. In addition the momentum of the reconstructed track was required to be within two standard deviations of the expectation for $K_{\mu 2}$ decays. There were over forty individual cuts associated with the beam and target pattern recognition as described in Section III B 2. The majority of the individual cuts had acceptance greater than 90% except for the delayed-coincidence (75.5%) and the CCDPUL (45.1%) requirements. The fourth row of Table IV contains the overall acceptance factor of the beam and target cuts.

To measure the acceptance of the Standard photon veto, an additional criterion was applied to the $K_{\mu 2}$ events used for the beam and target acceptance. As muons from $K_{\mu 2}$ decay can penetrate into the barrel veto, the reconstructed track was required to stop before the outermost layer of the range stack. The acceptance factor given in Table IV evaluated in this manner yielded the overall acceptance of both the online and offline photon veto cuts as the $K_{\mu 2}$ monitor trigger did not include the photon veto.

2. Acceptance factors from $K_{\pi 2}$ events

The $K_{\pi 2}$ monitor data were used to assess the acceptance factors associated with charged track reconstruction in the UTC and pion identification in the target. The acceptance of the veto of an additional track in the target (OPSVETO, Section III B 2) was also measured with $K_{\pi 2}$ monitors. The factors are listed in Table V and described below.

To measure the acceptance of the UTC reconstruction, events from the $K_{\pi 2}$ monitor trigger were required to

have a well-reconstructed track in the range stack and agreement between the online and offline determination of the range stack stopping counter. The factor is given in the second row of Table V.

For the measurement of the acceptance of the OPSVETO cut, in addition to the requirements described above, the charged track was required to be well-reconstructed in the UTC and range stack, identified as a π^+ from $K_{\pi 2}$ decay based on the measured range and momentum as well as the $\pi \to \mu \to e$ signature in the stopping counter and kinematically consistent with the pion from a $K_{\pi 2}$ decay. Cuts were also applied to ensure a single kaon entered the target. The acceptance factor for the OPSVETO is presented in the third row of Table V.

In addition to the requirements described above, the OPSVETO and target photon veto cuts were applied to the $K_{\pi 2}$ monitor events to assess the cumulative acceptance of the ten pion identification cuts in the target. These ten cuts were designed to reject tracks that contained an indication of a kink or discontinuity in the pattern of target fibers or target fibers with an unexpected energy deposit (Section III B 2). The acceptance factor for these cuts is listed in the fourth row of Table V. Two individual cuts with less than 90% acceptance were the requirement that no individual pion fiber had more than 3 MeV (89.6%) and the requirement on the target-track fitter probability $\mathcal{P}(\chi_5^2 + \chi_6^2 + \chi_7^2)$ (87.4%).

3. Acceptance factors from π_{scat} events

Beam pions that scatter in the target have a spectrum of range, energy and momentum similar to that of pions from $K^+ \to \pi^+ \nu \bar{\nu}$ and were used to determine the acceptance factors associated with the reconstruction and identification of pions in the range stack. Table VI lists the acceptance factors measured using π_{scat} monitors.

Candidate events were rejected if the pion stopped in a counter with a non-operational TD. The acceptance factor associated with this requirement was measured on a sample of π_{scat} monitor data selected by requiring a good outgoing track in the range stack, drift chamber, and target, a delayed coincidence of less than 5 ns, a single pion entering the target and range, energy and momentum in the signal region. The acceptance factor is given in the second row of Table VI.

In addition to the requirements listed above, π_{scat} mon-

itor data was also required to have a good $\pi \to \mu \to e$ signature and the pion was required to stop in range stack counter with an operational TD in order to measure the acceptance factor associated with the range stack kinematics and tracking. Assignment of target fibers to the incoming and outgoing pion in π_{scat} was not as robust as the assignments made for kaon decays at rest. Misassignment of target fibers yielded a larger uncertainty in the momentum, range and energy calculated for the outgoing pion in π_{scat} events. The effect of increasing or decreasing the signal phase space by ± 1 standard deviation was used to estimate the systematic uncertainty in this acceptance factor that is shown in third row of Table VI.

The requirements used to assess the acceptance factor associated with a non-operational TD in the stopping counter were supplemented by requiring a good track in the drift chamber and range and momentum consistent with a pion in order to measure the acceptance factor associated with the $\pi \to \mu \to e$ signature. The cut on the measured dE/dx in range stack counters and the cuts on the consistency of the range stack and drift chamber track had some correlation with the suite of cuts used to define the $\pi \to \mu \to e$ signature. The acceptance factor of the $\pi \to \mu \to e$ signature was assessed both with and without these cuts applied to estimate the systematic uncertainty due to these correlations. In addition a correction of $+1.4\%$ for pion decay-in-flight and pion absorption in the stopping counter, estimated from Monte Carlo, was applied to the acceptance factor associated with the $\pi \to \mu \to e$ signature as given in the fourth row of Table VI.

TABLE VI: Acceptance factors measured with π_{scat} monitor triggers. Operational is abbreviated as "Oper." The first and second uncertainties are statistical and systematic, respectively. The assessment of systematic uncertainties is described in the text. $A_{\pi_{\text{scat}}}$ is the product of the three acceptance factors.

Cut	Acceptance factor
Oper. TD in stopping counter	0.99843 ± 0.00010
Range stack kinematics	$0.82594 \pm 0.00126 \pm 0.01200$
$\pi \to \mu \to e$ signature	$0.4805 \pm 0.0015 \pm 0.0160$
$A_{\pi_{\text{scat}}}$	$0.3980 \pm 0.0014 \pm 0.0140$

4. Acceptance factors from simulated events

Simulated $K^+ \to \pi^+ \nu \bar{\nu}$ events were used to evaluate the trigger acceptance and the acceptance associated with phase space and π^+-nuclear interactions. The acceptance of the L1.1 and L1.2 (DC) components of the trigger as described in Section II B were evaluated with $K_{\pi 2}$ ($K_{\mu 2}$) monitors as described previously in this Section. The acceptance of the remaining trigger components is given in the second row of Table VII. The phase space acceptance of the events surviving the trigger simulation is shown in the third row of the Table. The phase

space acceptance includes the loss due to π^+ absorption in the stopping counter and decay in flight. Neither the trigger nor phase space acceptance include the effect of nuclear interactions. As indicated in Section III A, the combined trigger and phase space acceptance factor of 11.8% was larger than the corresponding factor of 6.5% for the $\pi \nu \bar{\nu}(1)$ region [2]. The acceptance factor associated with π^+-nuclear interactions was evaluated separately and is given in the fourth row of Table VII. For the $\pi \nu \bar{\nu}(1)$ region, the acceptance factor due to nuclear interactions was 49.5% [2].

TABLE VII: Acceptance factors determined from simulated $K^+ \to \pi^+ \nu \bar{\nu}$ decays. A_{MC} is the product of the three acceptance factors.

Component	Acceptance factor
Trigger	0.3225 ± 0.0015
Phase space	0.3650 ± 0.0027
π^+-nuclear interactions	0.8284 ± 0.0104
A_{MC}	0.0975 ± 0.0009

5. Correction to the $T \cdot 2 \cdot IC$ efficiency

The $T \cdot 2 \cdot IC$ component of the trigger (Section II B) required a coincidence between range stack counters in the same sector in the two innermost layers and in the IC. The simulation did not include the acceptance loss due to gaps between the neighboring T counters or due to insufficient scintillation light in the thin T counters. These acceptance losses were measured by using $K_{\mu 2}$ and $K_{\pi 2}$ decays in KB monitor events. The energy loss in the T counter by the charged track differs for $K_{\mu 2}$ and $K_{\pi 2}$ events and simulated events were used to obtain the average energy loss for each decay. The measured acceptance factors for $K_{\mu 2}$ and $K_{\pi 2}$ were then extrapolated to estimate

$$A_{T \cdot 2} = 0.9505 \pm 0.0012 \pm 0.0143 \quad (15)$$

where a $\pm 1.5\%$ systematic uncertainty was assigned to account for the extrapolation of the drift chamber track to the T counter.

6. Normalization to the $K_{\mu 2}$ branching ratio

We assessed the fraction (f_s) of K^+ that stopped in the target by normalization to the $K_{\mu 2}$ branching ratio [25] as described in [2]

$$f_s = 0.7740 \pm 0.0011 \quad . \quad (16)$$

7. Confirmation of the $K_{\pi 2}$ branching ratio

We measured the $K_{\pi 2}$ branching fraction using the $K_{\pi 2}$ monitor trigger data in order to confirm the validity of the acceptance factors and corrections calculated with data and Monte Carlo. Our measurement followed the same analysis procedure as described in [2] but utilized the selection criteria developed for the $\pi\nu\bar\nu(2)$ analysis. From this analysis we obtained

$$\mathcal{B}(K^+ \to \pi^+\pi^0) = 0.221 \pm 0.002 \qquad (17)$$

where the uncertainty is statistical. This is in reasonable agreement with the world average value [25] of 0.209 ± 0.001 for the branching fraction.

8. Overall acceptance and sensitivity

The total acceptance was evaluated as the product of $A_{K_{\pi 2}}$, $A_{K_{\mu 2}}$, $A_{\pi_{\mathrm{scat}}}$, A_{MC}, f_s and $A_{T \cdot 2}$ or $(1.37 \pm 0.14) \times 10^{-3}$ where we assigned a 10% uncertainty on the total acceptance to accommodate the discrepancy in $\mathcal{B}(K^+ \to \pi^+\pi^0)$ and the additional systematic and statistical uncertainties in the acceptance evaluated in this Section. Based on the total exposure of 1.71×10^{12} stopped kaons for this analysis, the single event sensitivity (SES) of the $\pi\nu\bar\nu(2)$ analysis was SES $= (4.28 \pm 0.43) \times 10^{-10}$ which can be compared with the SES of the E949 $\pi\nu\bar\nu(1)$ analysis of $(2.55 \pm 0.20) \times 10^{-10}$ [2] and the combined SES of the previous $\pi\nu\bar\nu(2)$ analyses of $(6.87 \pm 0.04) \times 10^{-10}$ with the E787 apparatus [35, 43].

E. Likelihood method

We determined $\mathcal{B}(K^+ \to \pi^+\nu\bar\nu)$ using a likelihood method that took into account the distributions of the predicted background and acceptance within the signal region. The signal region was divided into nine cells with differing acceptance-to-background ratios as described below. The likelihood ratio X was defined as

$$X \equiv \prod_{i=1}^{n} \frac{e^{-(s_i+b_i)}(s_i+b_i)^{d_i}}{d_i!} \bigg/ \frac{e^{-b_i}b_i^{d_i}}{d_i!} \qquad (18)$$

where s_i and b_i were the estimated signal and background in the ith cell, d_i was the observed number of signal candidates in the ith cell and n was the total number of cells [51]. The estimated signal in each cell was given by $s_i \equiv \mathrm{SES}_i \times \mathcal{B}(K^+ \to \pi^+\nu\bar\nu)$ where SES_i was the single event sensitivity of the ith cell.

The division of signal region into nine cells was performed using combinations of the decay pion kinematics (KIN), photon veto (PV), delayed coincidence (DC) or $\pi \to \mu \to e$ (TD) cuts. We defined a standard and a more

TABLE VIII: The estimated signal-to-background (s/b), background (b) and observed number of candidates for the nine cells. The cuts defining each cell are also given. The s/b is calculated assuming $\mathcal{B}(K^+ \to \pi^+\nu\bar\nu) = 1.73 \times 10^{-10}$. The uncertainties on b and s/b are omitted from the table. The definition column indicates the whether the tight version of the kinematics (KIN), photon veto (PV), delayed coincidence (DC) or $\pi \to \mu \to e$ (TD) cut or the inverted cut (i.e., $\overline{\mathrm{KIN}}$) was applied to define the cell. The cells containing signal candidate events A, B and C are indicated.

Cell definition	b	Candidates	s/b
$\mathrm{KIN} \cdot \mathrm{TD} \cdot \mathrm{DC} \cdot \mathrm{PV}$	0.152	0	0.84
$\mathrm{KIN} \cdot \overline{\mathrm{TD}} \cdot \mathrm{DC} \cdot \mathrm{PV}$	0.038	0	0.78
$\mathrm{KIN} \cdot \mathrm{TD} \cdot \overline{\mathrm{DC}} \cdot \mathrm{PV}$	0.019	0	0.66
$\mathrm{KIN} \cdot \overline{\mathrm{TD}} \cdot \overline{\mathrm{DC}} \cdot \mathrm{PV}$	0.005	0	0.57
$\mathrm{KIN} \cdot \mathrm{TD} \cdot \mathrm{DC} \cdot \overline{\mathrm{PV}}$	0.243	1 B	0.47
$\mathrm{KIN} \cdot \overline{\mathrm{TD}} \cdot \mathrm{DC} \cdot \overline{\mathrm{PV}}$	0.059	0	0.45
$\mathrm{KIN} \cdot \mathrm{TD} \cdot \overline{\mathrm{DC}} \cdot \overline{\mathrm{PV}}$	0.027	1 C	0.42
$\mathrm{KIN} \cdot \overline{\mathrm{TD}} \cdot \overline{\mathrm{DC}} \cdot \overline{\mathrm{PV}}$	0.007	0	0.35
$\overline{\mathrm{KIN}}$	0.379	1 A	0.20

restrictive or "tight" version of each cut as described previously. The signal region was defined by the application of the standard version of all cuts. The signal region was then subdivided into cells by the additional selective application of the tight version of each cut or the inverted cut as shown in Table VIII.

The additional signal acceptance factor and rejection (Table IX) for each of the four tight cuts was determined using analogous techniques and samples as described in Sections III D and III C, respectively. Based on studies of data and simulated events, we assumed that the background components for which no rejection is given in the Table were reduced by the acceptance factor of the particular cut. For example, the acceptance of the cell defined by $\mathrm{KIN} \cdot \overline{\mathrm{TD}} \cdot \overline{\mathrm{DC}} \cdot \mathrm{PV}$ relative to the acceptance for the entire signal region was $A_{\mathrm{KIN}} \times (1-A_{\mathrm{TD}}) \times (1-A_{\mathrm{DC}}) \times A_{\mathrm{PV}}$ with obvious notation and the $K_{\pi 2}$-target-scatter background component relative to the contribution to the entire signal region was reduced by the factor $1/R_{\mathrm{KIN}} \times (1-A_{\mathrm{TD}}) \times (1-A_{\mathrm{DC}}) \times 1/R_{\mathrm{PV}}$.

TABLE IX: Additional acceptance factor (A) or rejection (R) for the tight version of the kinematics (KIN), photon veto (PV), delayed coincidence (DC) or $\pi \to \mu \to e$ (TD) cuts for specific backgrounds.

	KIN	TD	DC	PV
A	0.812	0.812	0.911	0.522
R	1.63($K_{\pi 2}$)	3.08 (Muon)	6.3 (CEX)	2.75 ($K_{2(\gamma)}$)
	2.70(K_{e4})		1.0 (Beam)	
	1.20($K_{\pi 2\gamma}$)			

IV. RESULTS

In this Section, we describe the results of examining the signal region and the evaluation of the $K^+ \rightarrow \pi^+ \nu \bar{\nu}$ branching ratio. We also describe the evaluation of our observations within alternative models of $K^+ \rightarrow \pi^+ + nothing$.

A. Examination of the signal region

After completion of the background and acceptance analyses, all selection criteria were applied to the $\pi \nu \bar{\nu}(1+2)$ trigger data and three signal candidate events were selected. Some measured properties of the three events are listed in Table X and the cells containing candidates A, B and C are given in Table VIII. The kinetic

TABLE X: Range, energy and momentum of the π^+ in the signal candidate events A, B and C. The measured decay times are in units of K^+, π^+ and μ^+ lifetimes, appropriately.

Candidate	A	B	C
Momentum (MeV/c)	161.5	188.4	191.3
Range (cm)	17.3	24.2	26.1
Kinetic energy (MeV)	76.1	95.6	97.9
K^+ decay time	0.30	1.27	0.42
π^+ decay time	0.86	0.64	0.39
μ^+ decay time	2.71	1.03	4.33

energy vs. range of the three events along with the events found in the previous $\pi \nu \bar{\nu}(1)$ [2] and $\pi \nu \bar{\nu}(2)$ [35, 43] analyses are shown in Figure 16. The candidates's measured properties used in the selection criteria were consistent with the expected distributions for signal. There was no observed activity in the kaon fibers at the time of the π^+ for any of the three candidates according to the CCD-PUL analysis. The π^+ momentum of event A fails the KIN cut of 165 MeV/c. Events B and C fail the tight PV cut due to energy deposits of 2.4 and 2.1 MeV in the end cap above the 1.7 MeV threshold, respectively, and events A and C fail the tight DC cut of 6 ns on the kaon decay time.

B. The $K^+ \rightarrow \pi^+ \nu \bar{\nu}$ branching ratio

The central value of the $K^+ \rightarrow \pi^+ \nu \bar{\nu}$ branching ratio was taken to be the value of $\mathcal{B}(K^+ \rightarrow \pi^+ \nu \bar{\nu})$ that maximized X (Equation (18)) given the observed candidates. For the three events observed by this analysis, we determined $\mathcal{B}(K^+ \rightarrow \pi^+ \nu \bar{\nu}) = (7.89^{+9.26}_{-5.10}) \times 10^{-10}$ where the quoted 68% confidence level interval was determined from the behavior of X as described in [51] and took into account both the statistical and systematic uncertainties. The systematic uncertainties included the 10% uncertainty in the acceptance as well as the uncertainties in the estimation of the background components. The inclusion of systematic uncertainties had a negligible effect
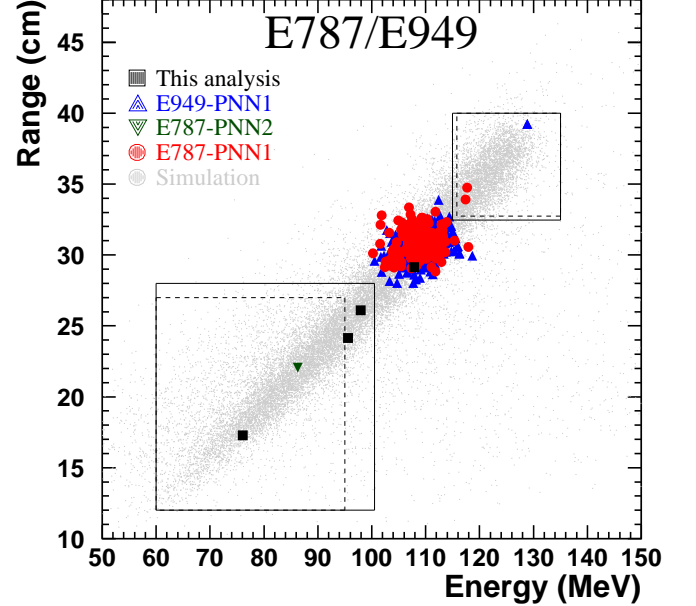

FIG. 16: Kinetic energy vs. range of all events passing all other cuts. The squares represent the events selected by this analysis. The circles and upward-pointing triangles represent the events selected by the E787 and E949 $\pi \nu \bar{\nu}(1)$ analyses, respectively. The downward-pointing triangles represent the events selected by the E787 $\pi \nu \bar{\nu}(2)$ analyses. The solid (dashed) lines represent the limits of the $\pi \nu \bar{\nu}(1)$ and $\pi \nu \bar{\nu}(2)$ signal regions for the E949 (E787) analyses. Despite the smaller signal region in E_π vs. R_π, the pnn1 analyses were 4.2 times more sensitive than the pnn2 analyses. The points near $E_\pi = 108$ MeV were $K_{\pi 2}$ decays that survived the photon veto cuts and were predominantly from the $\pi \nu \bar{\nu}(1)$ analyses due to the higher sensitivity and the less stringent photon veto cuts. The light gray points are simulated $K^+ \rightarrow \pi^+ \nu \bar{\nu}$ events that would be accepted by our trigger.

on the confidence level interval due to the poor statistical precision inherent in a three event sample. The probability that these three events were due to background only, given the estimated background in each cell (Table VIII), was 0.037.

When the results of the previous $\pi \nu \bar{\nu}(1)$ and $\pi \nu \bar{\nu}(2)$ analyses [2, 35, 43] were combined with the results of this analysis, we found $\mathcal{B}(K^+ \rightarrow \pi^+ \nu \bar{\nu}) = (1.73^{+1.15}_{-1.05}) \times 10^{-10}$ and $\mathcal{B}(K^+ \rightarrow \pi^+ \nu \bar{\nu}) < 3.35 \times 10^{-10}$ at 90% CL. Systematic uncertainties were treated as described above when performing the combination, except that we assumed a correlated 10% uncertainty for the acceptance assessed by each analysis. The probability that all seven events were due to background (background and standard model signal) was 0.001 (0.073).

The partial branching fraction for $K^+ \rightarrow \pi^+ \nu \bar{\nu}$ for two pion momentum regions is given in Table XI along with

the standard model prediction. The limits of the two

TABLE XI: The $K^+ \to \pi^+ \nu \bar{\nu}$ branching ratio measurements in units of 10^{-10}. The prediction was taken from [4] and scaled to the two pion momentum regions using the standard model spectral shape for $K^+ \to \pi^+ \nu \bar{\nu}$.

Momentum range (MeV/c)	Prediction	Measurement
[130, 205]	0.49 ± 0.04	$2.91^{+4.02}_{-1.79}$
[205, 227]	0.28 ± 0.02	$0.49^{+0.45}_{-0.29}$
All	0.85 ± 0.07	$1.73^{+1.15}_{-1.05}$

momentum regions were determined by the requirements on the reconstructed pion region and the detector resolution. The boundary between the two regions of 205 MeV/c was determined by lower and upper limits on the reconstructed π^+ momentum that were set to be approximately 2.5 standard deviations from the nominal $K_{\pi 2}$ momentum for the $\pi\nu\bar{\nu}(1)$ and $\pi\nu\bar{\nu}(2)$ analyses, respectively. The lower limit of 130 MeV/c was also determined by $\pi\nu\bar{\nu}(2)$ requirement on the reconstructed pion momentum. The upper limit of 227 MeV/c is the kinematic limit for the $K^+ \to \pi^+ \nu \bar{\nu}$ decay.

The 90% CL upper limit $\mathcal{B}(K^+ \to \pi^+ \nu \bar{\nu}) < 3.35 \times 10^{-10}$ can be used to calculate a model-independent upper limit of 14.6×10^{-10}, on the CP-violating process $K_L^0 \to \pi^0 \nu \bar{\nu}$[52]. This limit is substantially smaller than the current experimental limit of $\mathcal{B}(K_L^0 \to \pi^0 \nu \bar{\nu}) < 670 \times 10^{-10}$ [53].

C. Alternative model interpretations

The combined results of the E787 and E949 experiments have been interpreted assuming a scalar or tensor spectrum for the charged pion. The spectra are compared with the standard model spectrum in Figure 17. Using the same treatment of the data as for the standard model interpretation, the branching fraction for the scalar and tensor spectra were $\mathcal{B}_{sc}(K^+ \to \pi^+ \nu \bar{\nu}) = (9.9^{+8.5}_{-4.2}) \times 10^{-10}$ and $\mathcal{B}_{te}(K^+ \to \pi^+ \nu \bar{\nu}) = (4.9^{+3.9}_{-2.4}) \times 10^{-10}$, respectively, or $\mathcal{B}_{sc}(K^+ \to \pi^+ \nu \bar{\nu}) < 21 \times 10^{-10}$ and $\mathcal{B}_{te}(K^+ \to \pi^+ \nu \bar{\nu}) < 10 \times 10^{-10}$ at 90% CL.

The data have also been interpreted in the two-body decay model, $K^+ \to \pi^+ X$, where X was a massive non-interacting particle. The 90% CL upper limit on the branching ratio as a function of the mass of X is shown in Figure 18.

The limit in the Figure 18 can also be interpreted as a limit on the product of branching ratios $\mathcal{B}(K^+ \to \pi^+ P^0) \times \mathcal{B}(P^0 \to \nu \bar{\nu})$ for a hypothetical, short-lived particle P^0. The HyperCP collaboration observed three events consistent with $\Sigma^+ \to p P^0$ with $P^0 \to \mu^+ \mu^-$ having a mass $M(P^0) = 214.3 \pm 0.5$ MeV/c^2 [54]. A mass of 214.3 MeV/c^2 would correspond to a recoiling π^+ momentum of 170.1 MeV/c in a two-body K^+ decay. Of the four events in the $\pi\nu\bar{\nu}(2)$ region observed in E787 [43] and
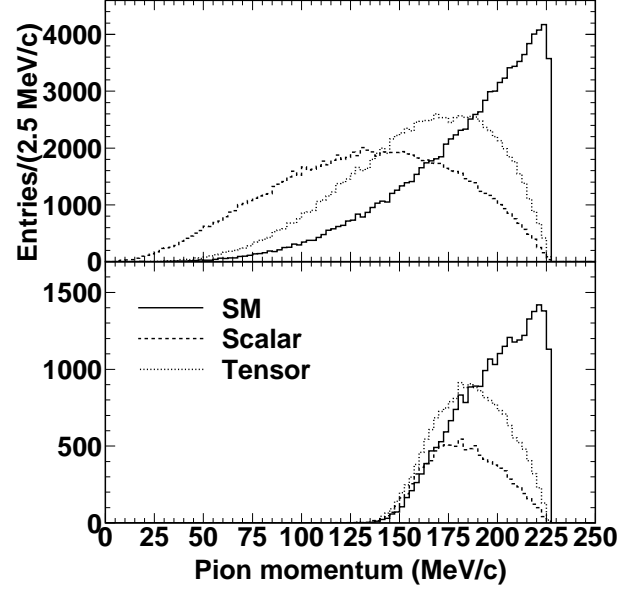

FIG. 17: (Top) The generated π^+ momentum spectrum for standard model (solid), scalar (dashed) and tensor (dotted) and scalar (dashed) momentum spectrum. (Bottom) The distributions for events passing the $\pi\nu\bar{\nu}(1+2)$ trigger.

E949, the closest was E949 candidate A that differed from the expected momentum by 3.7 standard deviations.

V. CONCLUSION

A. Summary

The rate of the decay $K^+ \to \pi^+ \nu \bar{\nu}$ is precisely predicted in the standard model to be $\mathcal{B}(K^+ \to \pi^+ \nu \bar{\nu}) = (0.85 \pm 0.07) \times 10^{-10}$ [4]. As the decay is a flavor-changing neutral current process and thus sensitive to new physics effects [7], it represents an opportunity to unambiguously probe for physics beyond the standard model.

The E787 and E949 experimental program at Brookhaven National Laboratory has demonstrated the feasibility of observation of the rare decay $K^+ \to \pi^+ \nu \bar{\nu}$ using a stopped-kaon experiment despite the poor experimental signature. The analysis presented in this article has established that backgrounds can be reduced to a reasonable level while maintaining signal acceptance to enable the $\pi\nu\bar{\nu}(2)$ region to be a viable supplement to the $\pi\nu\bar{\nu}(1)$ region [2] in the measurement of the $K^+ \to \pi^+ \nu \bar{\nu}$ branching ratio.
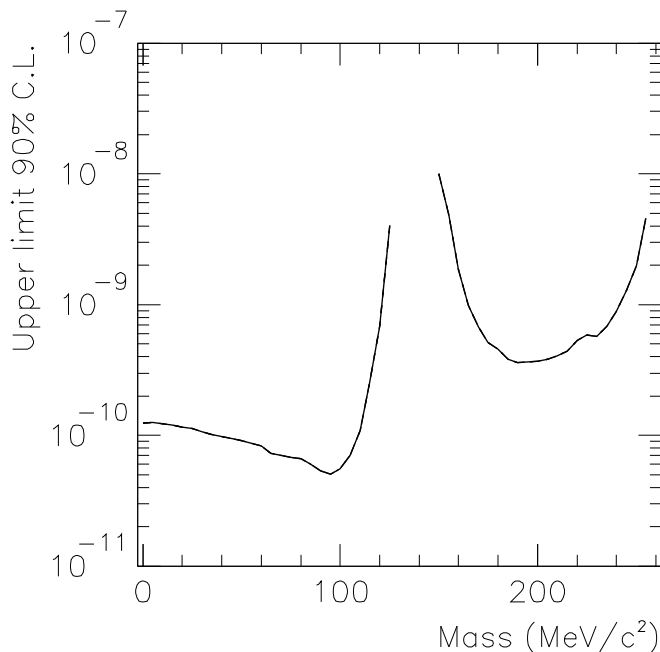
FIG. 18: The 90% CL upper limit on $\mathcal{B}(K^+ \to \pi^+ X)$ as a function of $M(X)$.

B. Future prospects

We briefly summarize the wisdom accumulated in the search for $K^+ \to \pi^+ \nu\bar{\nu}$ and the measurement of $\mathcal{B}(K^+ \to \pi^+ \nu\bar{\nu})$ in a stopped K^+ experiment:

1. Importance of blind analysis. The analysis procedure of concealing or obscuring the contents of the signal region are now well-established and widespread in particle physics [55]. The main benefit is to avoid or minimize bias in the selection criteria. This is particularly important for a rare process such as $K^+ \to \pi^+ \nu\bar{\nu}$ with a poor experimental signature that requires many individual cuts.

2. Use of data to estimate background and acceptance. In conjunction with the blinding of the signal region, the division of the data into 1/3 and 2/3 samples and the use of two powerful independent cuts provides background estimates that take into account instrumental effects not present in simulation and provides sensitivity to background beyond that of the $K^+ \to \pi^+ \nu\bar{\nu}$ sample as first noted in [33]. The bifurcation technique also permits examination of events that occur near the signal region as a means to validate the background estimates and investigate unforeseen sources of background.

3. Unforeseen acceptance losses. In the E787 proposal [56], only the $\pi\nu\bar{\nu}(1)$ analysis region was considered to be viable and the estimated acceptance was 1.5%. This can be compared to an E949 $\pi\nu\bar{\nu}(1)$ acceptance of 0.22% [2] and 0.14% for this analysis (Section III D). Acceptance was reduced due to

accidental activity that reduced the acceptance factors associated with vetoing and due to the cuts to suppress background that needed to be more stringent than anticipated.

4. Importance of redundancy and reliability in detector systems. In E949 and its predecessor E787, since nearly every detector element served as a veto of activity due to additional particles, the loss of any element represented a reduction in background rejection and motivated the redundant use of ADCs, TDCs and some form of waveform digitizer (CCDs or TDs). In addition, the positive identification of the π^+ by the $\pi \to \mu \to e$ decay chain required reliable operation of the TDs. If a pion stopped in a range stack counter with a non-operational TD, the data were discarded resulting in a loss of sensitivity. In E949 we improved the TD reliability to 99.8% (Table VI) compared to 97.3% in E787 after installation of LED flasher monitoring system [49].

5. Need for 4-π sr photon veto coverage. The early $K^+ \to \pi^+ \nu\bar{\nu}$ counter experiments showed the benefits of photon veto capability over the full 4-π sr solid angle [28, 29]. Each modification or upgrade of the original E787 experiment included photon veto enhancements. For example, E949 contained upgrades with respect to E787 that sought to further suppress the contribution of the $K_{\pi 2}$ background to both the $\pi\nu\bar{\nu}(1)$ and $\pi\nu\bar{\nu}(2)$ analyses. The barrel veto liner (BVL) improved the photon veto rejection in the barrel region by a factor of 2 and the active degrader (AD) increased the photon veto rejection for the $\pi\nu\bar{\nu}(2)$ analysis by 1.95 (Section III B 5).

Extrapolating from the E787 and E949 experience, a stopped K^+ experiment that could yield hundreds of detected $K^+ \to \pi^+ \nu\bar{\nu}$ decays [57] would entail the following improvements:

1. Higher intensity proton beam with 100% duty factor,

2. A lower momentum, larger acceptance (450 MeV/c) K^+ beam with a higher stopping fraction,

3. Higher magnetic field (3T) for a more compact detector and ×2 improvement in momentum resolution

4. Finer segmentation (×150 elements, ∼5-mm square fibers) of the range stack,

5. A more hermetic, fully active liquid xenon photon veto with more radiation lengths,

6. A longer magnet, allowing more solid angle acceptance, and

7. A short target with double-ended readout to provide better discrimination against $K_{\pi 2}$ target-scatter background.

[1] A. Artamanov et al., Phys. Rev. Lett. **101**, 191802 (2008), arXiv:0808.2459.
[2] S. Adler et al., Phys. Rev. **D77**, 052003 (2008), arXiv:0709.1000.
[3] M. K. Gaillard and B. W. Lee, Phys. Rev. **D10**, 897 (1974).
[4] J. Brod and M. Gorbahn, Phys. Rev. **D78**, 034006 (2008).
[5] N. Cabibbo, Phys. Rev. Lett. **10**, 531 (1963).
[6] M. Kobayashi and T. Maskawa, Prog. Theor. Phys. **49**, 652 (1973).
[7] A. J. Buras, F. Schwab, and S. Uhlig, Rev. Mod. Phys. **80**, 965 (2008), hep-ph/0405132.
[8] M. Blanke, A. J. Buras, S. Recksiegel, and C. Tarantino (2008), 0805.4393.
[9] T. Goto, Y. Okada, and Y. Yamamoto (2008), 0809.4753.
[10] P. N. Kopnin and M. I. Vysotsky, JETP Lett. **87**, 517 (2008), 0804.0912.
[11] T. Hurth, G. Isidori, J. F. Kamenik, and F. Mescia (2008), 0807.5039.
[12] T. Appelquist, N. D. Christensen, M. Piai, and R. Shrock, Phys. Rev. **D70**, 093010 (2004), hep-ph/0409035.
[13] Y. Grossman, G. Isidori, and H. Murayama, Phys. Lett. **B588**, 74 (2004), hep-ph/0311353.
[14] C.-H. Chen, C.-Q. Geng, and T.-C. Yuan, Phys. Rev. **D75**, 077301 (2007), hep-ph/0703196.
[15] A. Deandrea, J. Welzel, and M. Oertel, JHEP **10**, 038 (2004), hep-ph/0407216.
[16] M. Hindmarsh and P. Moulatsiotis, Phys. Rev. **D59**, 055015 (1999), hep-ph/9807363.
[17] F. Wilczek, Phys. Rev. Lett. **49**, 1549 (1982).
[18] D. S. Gorbunov, Nucl. Phys. **B602**, 213 (2001), hep-ph/0007325.
[19] T. M. Aliev, M. I. Dobroliubov, and A. Y. Ignatiev, Nucl. Phys. **B335**, 311 (1990).
[20] M. Pospelov (2008), 0811.1030.
[21] M. Pospelov, A. Ritz, and M. B. Voloshin, Phys. Lett. **B662**, 53 (2008), 0711.4866.
[22] P. Fayet, Phys. Rev. **D75**, 115017 (2007), hep-ph/0702176.
[23] J. F. Gunion, D. Hooper, and B. McElrath, Phys. Rev. **D73**, 015011 (2006), hep-ph/0509024.
[24] Y. Wu and D.-X. Zhang (2008), 0804.1843.
[25] W. M. Yao et al., J. Phys. **G33**, 1 (2006).
[26] U. Camerini, D. Ljung, M. Sheaff, and D. Cline, Phys. Rev. Lett. **23**, 326 (1969).
[27] D. Ljung and D. Cline, Phys. Rev. **D8**, 1307 (1973).
[28] G. D. Cable, R. H. Hildebrand, C. Y. Pang, and R. Stiening, Phys. Rev. **D8**, 3807 (1973).
[29] C. Y. Pang, R. H. Hildebrand, G. D. Cable, and R. Stiening, Phys. Rev. **D8**, 1989 (1973).
[30] M. S. Atiya et al., Phys. Rev. **D48**, 1 (1993).
[31] F. Mescia and C. Smith, Phys. Rev. **D76**, 034017 (2007), arXiv:0705.2025.
[32] J. Roy, Ph.D. thesis, University of British Columbia (1994).
[33] M. S. Atiya et al., Phys. Rev. Lett. **70**, 2521 (1993).
[34] S. S. Adler et al. (E787), Phys. Lett. **B537**, 211 (2002), hep-ex/0201037.
[35] S. Adler et al., Phys. Rev. **D70**, 037102 (2004), hep-ex/0403034.
[36] B. Bhuyan, Ph.D. thesis, University of Delhi (2003).
[37] B. Bassalleck et al. (1999), BNL-67247, TRI-PP-00-06.
[38] D. A. Bryman et al., Nucl. Instrum. Meth. **A396**, 394 (1997).
[39] M. Atiya, M. Ito, J. Haggerty, C. Ng, and F. W. Sippach, Nucl. Instrum. Meth. **A279**, 180 (1989).
[40] E. W. Blackmore et al., Nucl. Instrum. Meth. **A404**, 295 (1998).
[41] I. H. Chiang et al., IEEE Trans. Nucl. Sci. **42**, 394 (1995).
[42] T. K. Komatsubara et al., Nucl. Instrum. Meth. **A404**, 315 (1998).
[43] S. Adler et al., Phys. Lett. **B537**, 211 (2002), hep-ex/0201037.
[44] I.-A. Christidi, Ph.D. thesis, Stony Brook University (2006).
[45] M. Piccini, J. Phys. Conf. Ser. **110**, 042021 (2008), The interference term was found to have roughly the same magnitude as direct emission in these preliminary results.
[46] K. Mizouchi, Ph.D. thesis, Kyoto University (2006).
[47] M. Ardebili, Ph.D. thesis, Princeton University (1995), UMI-95-27860.
[48] W. R. Nelson, H. Hirayama, and D. W. O. Rogers (1985), SLAC-0265.
[49] B. Lewis, Ph.D. thesis, The University of New Mexico (2007).
[50] This method of assigning systematic uncertainty was intended to define a range that included the actual value of the background.
[51] T. Junk, Nucl. Instrum. Meth. **A434**, 435 (1999), hep-ex/9902006.
[52] Y. Grossman and Y. Nir, Phys. Lett. **B398**, 163 (1997), hep-ph/9701313.

[53] J. K. Ahn et al. (E391a), Phys. Rev. Lett. **100**, 201802 (2008), 0712.4164.

[54] H. Park et al. (HyperCP), Phys. Rev. Lett. **94**, 021801 (2005), hep-ex/0501014.

[55] J. R. Klein and A. Roodman, Ann. Rev. Nucl. Part. Sci. **55**, 141 (2005).

[56] I.-H. Chiang et al. (1983), BNL AGS Proposal.

[57] J. Appel et al. (2008), http://www.fnal.gov/directorate/Longrange/Steering_Public/P